Cell Reports

Article

Blocking AMPK β1 myristoylation enhances AMPK activity and protects mice from high-fat diet-induced obesity and hepatic steatosis

Graphical abstract

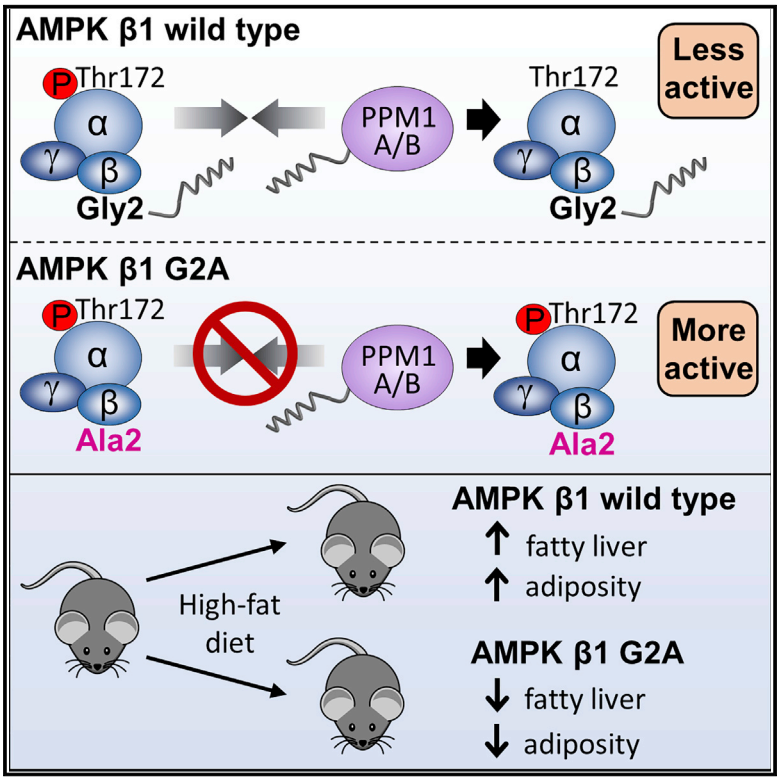

Highlights

- Generation of mice carrying a myristoylation-deficient G2A mutation of AMPKβ1
- AMPKβ1 G2A cells have increased basal AMPKα Thr172 phosphorylation and activity
- Blocking AMPKβ1 myristoylation disrupts colocalization with the phosphatase PPM1A/B
- AMPKβ1 G2A mice have improved metabolic health under high-fat diet conditions

Authors

Katyayanee Neopane, Natalie Kozlov, Florentina Negoita, ..., Bruce E. Kemp, Kei Sakamoto, Sandra Galic

Correspondence

kei.sakamoto@sund.ku.dk (K.S.), sgalic@svi.edu.au (S.G.)

In brief

Neopane et al. show that genetic loss of the AMPK β1 myristoylation site (G2A) disrupts colocalization with the phosphatase PPM1A/B. Cells expressing non-myristoylated AMPK β1-G2A have increased basal AMPK activity despite reduced stability of the β1 subunit. High-fat diet-fed AMPK β1-G2A mice have reduced liver lipid accumulation and improved insulin sensitivity.

Neopane et al., 2022, Cell Reports *41*, 111862
December 20, 2022
https://doi.org/10.1016/j.celrep.2022.111862

CellPress

Cell Reports

CellPress
OPEN ACCESS

Article

Blocking AMPK β1 myristoylation enhances AMPK activity and protects mice from high-fat diet-induced obesity and hepatic steatosis

Katyayanee Neopane,[1,2,14] Natalie Kozlov,[3,14] Florentina Negoita,[4] Lisa Murray-Segal,[3] Robert Brink,[5] Ashfaqul Hoque,[6] Ashley J. Ovens,[6] Gavin Tjin,[7,9] Luke M. McAloon,[8] Dingyi Yu,[3] Naomi X.Y. Ling,[6] Matthew J. Sanders,[1] Jonathan S. Oakhill,[6,9] John W. Scott,[8,10] Gregory R. Steinberg,[11] Kim Loh,[9,12] Bruce E. Kemp,[3,9,13] Kei Sakamoto,[4,15,*] and Sandra Galic[3,9,15,16,*]

[1]Nestlé Institute of Health Sciences, Nestlé Research, Société des Produits Nestlé S.A., 1015 Lausanne, Switzerland
[2]School of Life Sciences, École Polytechnique Fédérale de Lausanne, Lausanne 1015, Switzerland
[3]Protein Chemistry and Metabolism, St. Vincent's Institute of Medical Research, Melbourne, VIC 3065, Australia
[4]Novo Nordisk Foundation Center for Basic Metabolic Research, University of Copenhagen, Copenhagen 2200, Denmark
[5]Garvan Institute of Medical Research and St. Vincent's Clinical School, University of New South Wales, Sydney, Darlinghurst, NSW 2010, Australia
[6]Metabolic Signalling, St. Vincent's Institute of Medical Research, Fitzroy, VIC 3065, Australia
[7]Stem Cell Regulation, St. Vincent's Institute of Medical Research, Fitzroy, VIC 3065, Australia
[8]Drug Discovery Biology, Monash Institute of Pharmaceutical Sciences, Parkville, VIC 3052, Australia
[9]Department of Medicine, University of Melbourne, Parkville, VIC 3010, Australia
[10]The Florey Institute of Neuroscience and Mental Health, Parkville, Melbourne, VIC 3052, Australia
[11]Centre for Metabolism, Obesity, and Diabetes Research, Departments of Medicine and Biochemistry and Biomedical Sciences, McMaster University, Hamilton, ON, Canada
[12]Diabetes and Metabolic Disease, St. Vincent's Institute of Medical Research, Fitzroy, VIC 3065, Australia
[13]Mary McKillop Institute for Health Research, Australian Catholic University, Melbourne 3000, VIC, Australia
[14]These authors contributed equally
[15]Senior author
[16]Lead contact
*Correspondence: kei.sakamoto@sund.ku.dk (K.S.), sgalic@svi.edu.au (S.G.)
https://doi.org/10.1016/j.celrep.2022.111862

SUMMARY

AMP-activated protein kinase (AMPK) is a master regulator of cellular energy homeostasis and a therapeutic target for metabolic diseases. Co/post-translational N-myristoylation of glycine-2 (Gly2) of the AMPK β subunit has been suggested to regulate the distribution of the kinase between the cytosol and membranes through a "myristoyl switch" mechanism. However, the relevance of AMPK myristoylation for metabolic signaling in cells and *in vivo* is unclear. Here, we generated knockin mice with a Gly2-to-alanine point mutation of AMPKβ1 (β1-G2A). We demonstrate that non-myristoylated AMPKβ1 has reduced stability but is associated with increased kinase activity and phosphorylation of the Thr172 activation site in the AMPK α subunit. Using proximity ligation assays, we show that loss of β1 myristoylation impedes colocalization of the phosphatase PPM1A/B with AMPK in cells. Mice carrying the β1-G2A mutation have improved metabolic health with reduced adiposity, hepatic lipid accumulation, and insulin resistance under conditions of high-fat diet-induced obesity.

INTRODUCTION

AMP-activated protein kinase (AMPK) is a cellular energy sensor that is activated by low-energy conditions and phosphorylates a wide range of substrates, including key metabolic proteins and transcription factors, to restore energy homeostasis.[1] In response to a cellular energy deficit signaled by an increase in the AMP/ATP ratio, AMPK redirects metabolism away from ATP-consuming processes and promotes ATP-generating pathways, allowing the cell to match its activity with the available energy supply. For example, AMPK-mediated phosphorylation and inhibition of 3-hydroxy-3-methylglutaryl coenzyme A (HMG-CoA) reductase and acetyl-CoA carboxylase (ACC) suppresses the energy-consuming reactions of cholesterol and fatty acid synthesis, respectively.[2,3] Concomitant with reduced fatty acid synthesis, AMPK-mediated reduction of intracellular malonyl-CoA levels, the product of the ACC-catalyzed reaction, reduces malonyl-CoA inhibition of mitochondrial carnitine palmitoyl transferase-1 and stimulation of ATP generation through fatty acid β-oxidation. AMPK regulates the activity of a multitude of metabolic and non-metabolic substrates, including key proteins involved in glucose metabolism, protein synthesis, mitochondrial biogenesis, autophagy, and cell

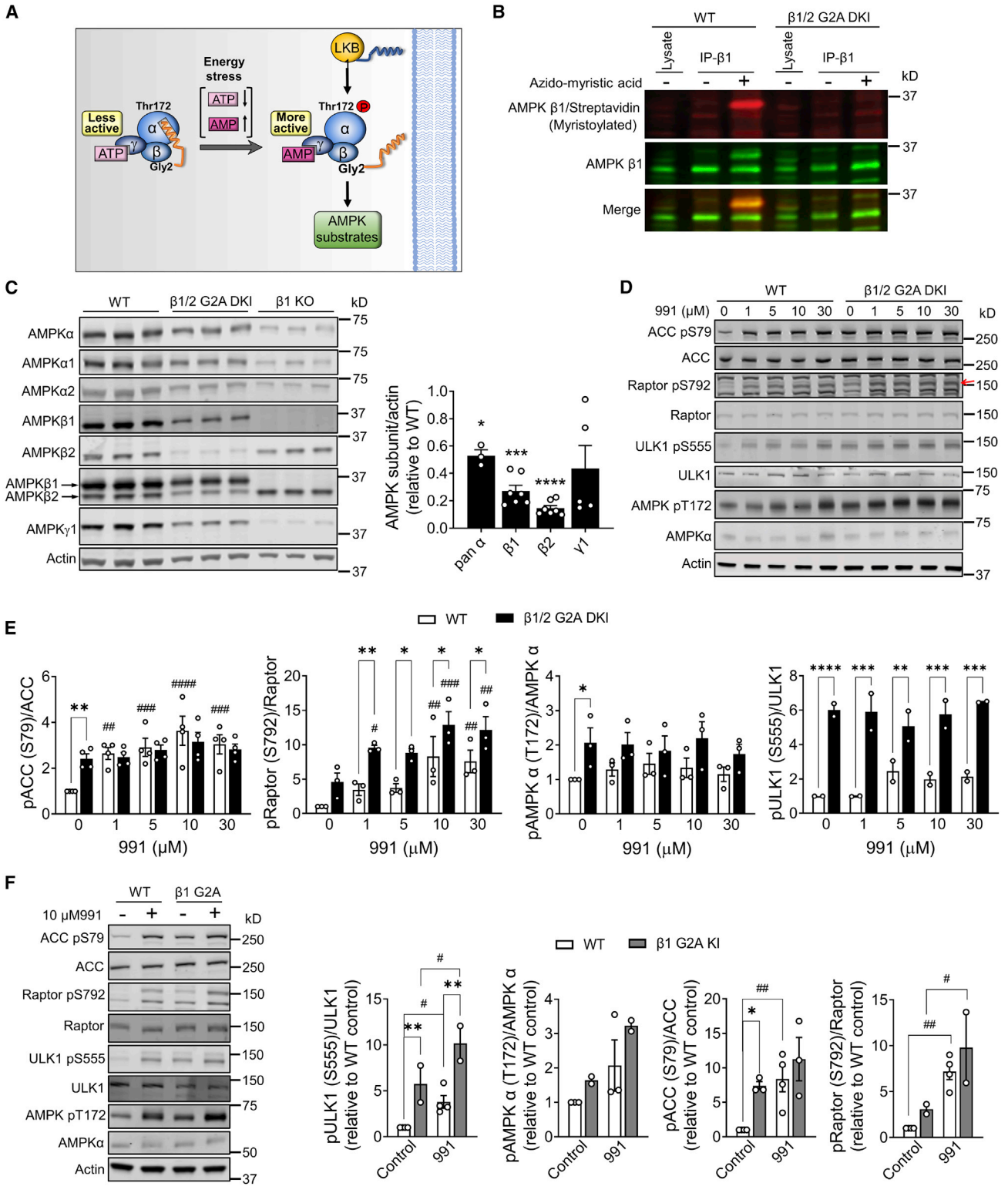

Figure 1. Lack of AMPKβ Gly-2 myristoylation results in enhanced AMPK phosphorylation and activity in cells

(A) Currently proposed role of AMPK β-Gly2 myristoylation in AMPK signaling. AMP binding to the γ-subunit triggers myristoyl group extrusion, promoting AMPK localization at intracellular membranes and facilitating engagement with other lipidated signaling proteins. This myristoyl switch promotes α-Thr172

(legend continued on next page)

proliferation. Studies using genetic and pharmacologic modulation of AMPK activity *in vivo* have also demonstrated a pivotal role of AMPK as a key regulator of whole-body energy metabolism, linking AMPK activation to improved exercise capacity and glucose disposal and suppression of obesity, hepatic steatosis, and inflammation.[4–6] These findings highlight AMPK's potential as a pharmacological target for metabolic diseases, including type 2 diabetes, cardiovascular disease, and obesity, and emphasize the need for a better understanding of the structural, molecular, and physiological determinants of AMPK action.

AMPK is a heterotrimeric complex consisting of a catalytic α subunit and two regulatory subunits, β and γ, each with different isoforms (α1, α2, β1, β2, γ1, γ2, and γ3) and encoded by separate genes.[7,8] The α subunit contains the catalytic domain that is, under physiological conditions, activated by phosphorylation of Thr172 by upstream kinases, including liver kinase B1 (LKB1) and calcium-calmodulin-dependent kinase kinase-2 (CaMKK2).[7,8] Conversely, AMPK is inactivated by Thr172 dephosphorylation by protein phosphatases, including members of the phosphoprotein phosphatases and metal-dependent protein phosphatase (PPM) family (such as PPM1A and PPM1B, also known as PP2Cα/β) and protein phosphatase 2A (PP2A).[9–12] AMPK is also activated allosterically, which is mediated by binding of AMP to three nucleotide-binding sites of the γ subunit. Binding of AMP and ADP helps maintain AMPK activity by protecting Thr172 from dephosphorylation.[10,11,13] The C-terminal sequence of the β subunit functions to anchor α and γ subunits for assembly of the AMPK heterotrimer core, whereas a central carbohydrate-binding module (CBM) permits AMPK association with glycogen.[14,15] The β subunit also undergoes N-terminal myristoylation of Gly2, which occurs in the β1 and β2 isoforms.[16–18] N-myristoylation is a ubiquitous, generally co-translational modification of newly synthesized proteins that involves attachment of the C14 fatty acid (myristic acid) to the N-terminal glycine. The reaction is catalyzed by the enzyme N-myristoyl transferase (NMT), to date only found in eukaryotic cells. Numerous studies have confirmed the importance of myristoylation for facilitation of protein-protein interactions and protein-membrane associations with profound effects on protein stability and signal transduction.[19–21] AMPK was among the first proteins discovered to undergo N-myristoylation,[22] but its role in AMPK function in cells and *in vivo* remains poorly understood. Research to date suggests that this modification facilitates AMPK association with intracellular membranes in response to increased levels of AMP and nutrient stress, suggesting that, similar to other myristoylated proteins, AMPK may undergo a ligand-induced "myristoyl switch" between membrane-bound and cytoplasmic forms[17,18] (Figure 1A). Such a mechanism may allow AMPK to effectively sense and transduce energy stress signals by enabling interaction with membrane-bound signaling proteins. Although an AMPK myristoyl switch hypothesis has not been unequivocally validated, several subsequent studies confirmed the importance of the myristoyl group for AMPK association with lysosomal[23,24] and mitochondrial[25] membranes and phosphorylation by kinases, including LKB1[24] and Unc-51-like kinase 1 (ULK1).[26]

Despite indications that myristoylation is an important component of AMPK function, the role of β subunit myristoylation at the whole-organism level remains unknown. In the current study, we generated mice with whole-body alanine knockin mutations of the myristoylation site Gly2 of the β subunit and focused on investigating the importance of β1 isoform myristoylation for metabolic signaling and outcomes *in vivo*. We found that loss of myristoylation prevented colocalization of PPM1A/B to AMPK and resulted in increased basal phosphorylation of α-Thr172 and AMPK substrates in cells. These changes were associated with reduced adiposity, hepatic lipid accumulation, and protection from high-fat diet-induced insulin resistance, demonstrating that disruption of AMPK myristoylation has striking beneficial effects on metabolic health.

RESULTS

Ablation of AMPK β Gly-2 myristoylation enhances cellular AMPK activity

To investigate the role of AMPK β subunit myristoylation in regulation of endogenous AMPK function, we used CRISPR-Cas9 gene targeting to generate two whole-body knockin (KI) mouse lines on a C57BL/6 background carrying glycine-2-to-alanine (G2A) point mutations of the β1 (Figure S1A) and β2 (Figure S1B) subunits, respectively. We intercrossed these strains to generate AMPK β1/β2-G2A double KI (DKI) mice, which were subsequently used for isolation of β1/β2-G2A DKI mouse embryonic fibroblasts (MEFs). To verify that myristoylation of endogenous AMPK β1, the predominant β isoform in MEFs, was detectable

phosphorylation and activation of AMPK via the prenylated AMPK kinase LKB1 and may be required for effective transduction of energy stress signals by targeting AMPK to membrane-associated substrates.

(B) Wild-type (WT) or AMPK β1/2-G2A double-knockin (DKI) mouse embryonic fibroblasts (MEFs) were incubated with azido-myristic acid (25 μM) for 24 h. AMPK β1 was immunoprecipitated, and a click chemistry reaction was performed using biotin-alkyne followed by immunoblot analysis. Myristoylated and total β1 was detected by streptavidin-AF680 or total β1 antibody and visualized using the LI-COR Biosciences Odyssey Blot Imager. Data shown are representative immunoblots from three independent experiments.

(C) Immunoblots of the AMPK subunit isoforms in WT, β1/2-G2A DKI, and β1 knockout (KO) MEFs and quantification of AMPK subunit isoform expression in β1/2-G2A DKI MEFs relative to the WT. The immunoblots shown are representative of three independent experiments.

(D and E) Immunoblots (D) and quantification (E) of phosphorylation of AMPK and its substrates in the presence or absence of increasing concentrations of 991 for 30 min in WT or β1/2-G2A DKI MEFs. The phospho-signal was normalized to respective total protein and expressed as relative to the vehicle-treated WT. A red arrow indicates the band of interest.

(F) WT or β1-G2A KI MEFs were treated with 10 μM 991 for 30 min and lysed for immunoblot analysis. Shown are representative immunoblots from two independent experiments.

*$p < 0.05$, **$p < 0.01$, ***$p < 0.001$, and ***$p < 0.0001$ indicate differences between genotypes. #$p < 0.05$, ##$p < 0.01$, ###$p < 0.001$, and ####$p < 0.0001$ represent 991 effects compared with vehicle control as determined by unpaired Student's t test (C) or two-way ANOVA with Šídák's post hoc test. All data are mean ± SEM. See also Figures S1 and S2.

in wild-type (WT) but absent in β1/β2-G2A DKI MEFs, we took a click chemistry approach.[27] MEFs were treated with increasing doses of azido-myristic acid (5–50 μM) for up to 24 h, followed by immunoprecipitation and visualization of myristoylated AMPK β1 by immunoblotting (Figures S2A and S2B). We observed that AMPK β1 was most robustly myristoylated (>50% of total β1) when cells were incubated with azido-myristic acid at 25 μM or greater for 24 h. Under this condition, we confirmed that myristoylation of β1 was only detectable in WT but not in β1/β2-G2A DKI MEFs (Figure 1B).

Analysis of AMPK subunit/isoform expression in AMPK β1/β2-G2A DKI MEFs revealed that α, β1, and β2 subunit protein levels were reduced by ~50%, 75%, and 90%, respectively, indicating a protective effect of β subunit myristoylation on AMPK protein stability (Figure 1C). To determine whether the stoichiometry of AMPK heterotrimer formation was retained in the G2A mutant, we immunoprecipitated AMPK β1 from β1/β2-G2A DKI MEF lysates and analyzed the presence of AMPK subunits in the pull-down. We confirmed that relative interaction of β1 with α and γ subunits was comparable between the WT and G2A mutant (Figure S2C). To investigate the effect of AMPK β myristoylation on AMPK activity and signaling in cells, we left WT and β1/β2-G2A DKI MEFs untreated or treated them with increasing doses of the specific allosteric AMPK activator 991[28,29] for 30 min. 991 robustly increased phosphorylation of AMPK substrates, including ACC, Raptor, and ULK1, in WT MEFs (Figures 1D and 1E). In contrast, phosphorylation of AMPK α and its substrates was markedly higher in untreated β1/β2-G2A DKI compared with WT cells, with only modest changes in phosphorylation of AMPK α and its substrates with 991 treatment (Figures 1D and 1E). Consistent with these observations, AMPK β1 activity under the untreated/basal condition was ~3-fold higher in β1/β2-G2A DKI compared with WT MEFs (Figure S2D). We also analyzed MEFs derived from AMPK β1-G2A single KI mice and observed enhanced phosphorylation of ACC and ULK1 in the untreated/basal state (Figure 1F). In contrast, signaling in AMPK β2-G2A single KI MEFs was similar to results obtained in WT cells (Figure S2E), indicating a predominant contribution of AMPK β1 complexes to the signaling phenotype of β1/β2-G2A DKI MEFs. These data show that loss of AMPK β1 myristoylation is associated with enhanced AMPK α Thr172 phosphorylation and activity of endogenous AMPK in cells.

Blocking AMPK β1 Gly-2 myristoylation disrupts colocalization with PPM1A/B

To exclude the possibility that the altered signaling of the AMPK β1-G2A mutant was a consequence of intrinsic myristoylation-independent effects of the G2A mutation, we performed biochemical and biophysical analyses of purified AMPK WT α1β1γ1 and mutant α1β1(G2A)γ1 complexes expressed in *E. coli* (Figure S3A). Bacterially expressed AMPK WT complexes are not myristoylated, allowing direct comparisons with the β1-G2A mutant solely based on the presence of Gly or Ala in position 2. The β1-G2A mutation, confirmed by time-of-flight mass spectrometry (Figure S3B), had no effect on AMPK complex melting temperature compared with the WT (Figure S3C). *In vitro* CaMKK2 phosphorylation kinetics analysis demonstrated that WT and β1-G2A complexes are phosphorylated on α-Thr172 at identical rates, indicating appropriate exposure and conformation of the AMPKα kinase domain activation loop (Figure S3D). These data provide evidence that the Ala mutation does not intrinsically affect AMPK global or local structural conformation and regulation, and that effects in MEFs are likely attributable to loss of β-myristoylation.

To investigate whether loss of AMPK β1-G2A myristoylation was associated with changes in subcellular membrane localization, we performed immunofluorescence analysis of AMPK β1 co-occurrence with the lysosomal marker LAMP1 in β1/β2-G2A DKI MEFs (Figure S4A). The specificity of the AMPK β1 antibody was confirmed using β1 knockout (KO) MEFs (Figure S4A). Consistent with our previous study,[17] we found that β1 was widely distributed across the cytosol, whereas LAMP1 showed the expected punctate and largely perinuclear staining. Intensity-based colocalization analyses revealed a modest reduction in the fraction of AMPK β1 fluorescence colocalizing with LAMP1 fluorescence in AMPK β1-G2A MEFs (overall genotype effect, $p < 0.001$) (Figure S4A), suggesting that, in agreement with previous reports,[17,18,23,24] β subunit myristoylation may facilitate AMPK targeting to intracellular membranes. Myristoylation and translocation of AMPK to the lysosome membrane have been suggested previously to be a prerequisite for AMP-induced phosphorylation and activation by LKB1.[24] However, cell treatment with 5-aminoimidazole-4-carboxamide ribonucleotide (AICAR), a pro-drug for the AMP analog ZMP, had no overall measurable effect on AMPK β1/LAMP1 signal colocalization (Figure S4A), despite clear effects on AMPK α-Thr172 and substrate phosphorylation (Figure S4B). It is therefore likely that the potentiating effect of the G2A mutation on AMPK signaling in β1/β2-G2A DKI MEFs is independent of its effects on lysosomal targeting and localization with LKB1.

We next hypothesized that enhanced AMPK α-Thr172 phosphorylation coupled with increased cellular AMPK activity observed in β1/β2-G2A DKI MEFs was due to disrupted colocalization with AMPK phosphatases. It has been reported previously that PPM1A and PPM1B are myristoylated in HeLa cells.[9] To verify that PPM1A and PPM1B are also myristoylated in MEFs, we performed a click chemistry analysis in WT MEFs transfected with small interfering RNA (siRNA) targeting PPM1A or PPM1B or siRNA with a nonsense/scrambled sequence as a control. We detected myristoylated PPM1A and PPM1B in non-transfected and control siRNA-transfected MEFs in the presence of myristic acid (Figure 2A). In contrast, myristoylation of PPM1A and PPM1B was ablated in cells transfected with siRNA targeting PPM1A or PPM1B (Figure 2A).

We next examined whether AMPK β1 and PPM1A/PPM1B co-localize in cells. We took advantage of the proximity ligation assay, which permits visualization and quantification of protein-protein interactions *in situ* at endogenous protein levels.[30] As shown in Figure 2B, under fluorescence microscopy, we observed a cluster of signals (dots) enriched in WT MEFs, indicating proximity of AMPK β1 and PPM1A/PPM1B. The specificity of this interaction was verified; depletion of PPM1B by siRNA (Figure S4C) resulted in ablation of the signals/dots (Figure S4D). The number of dots as well as the mean intensity of the fluorescence signal was significantly reduced in AMPK β1/β2-DKI and absent in AMPK β1 KO MEFs (Figure 2B). This is consistent with a previous study, where ectopic

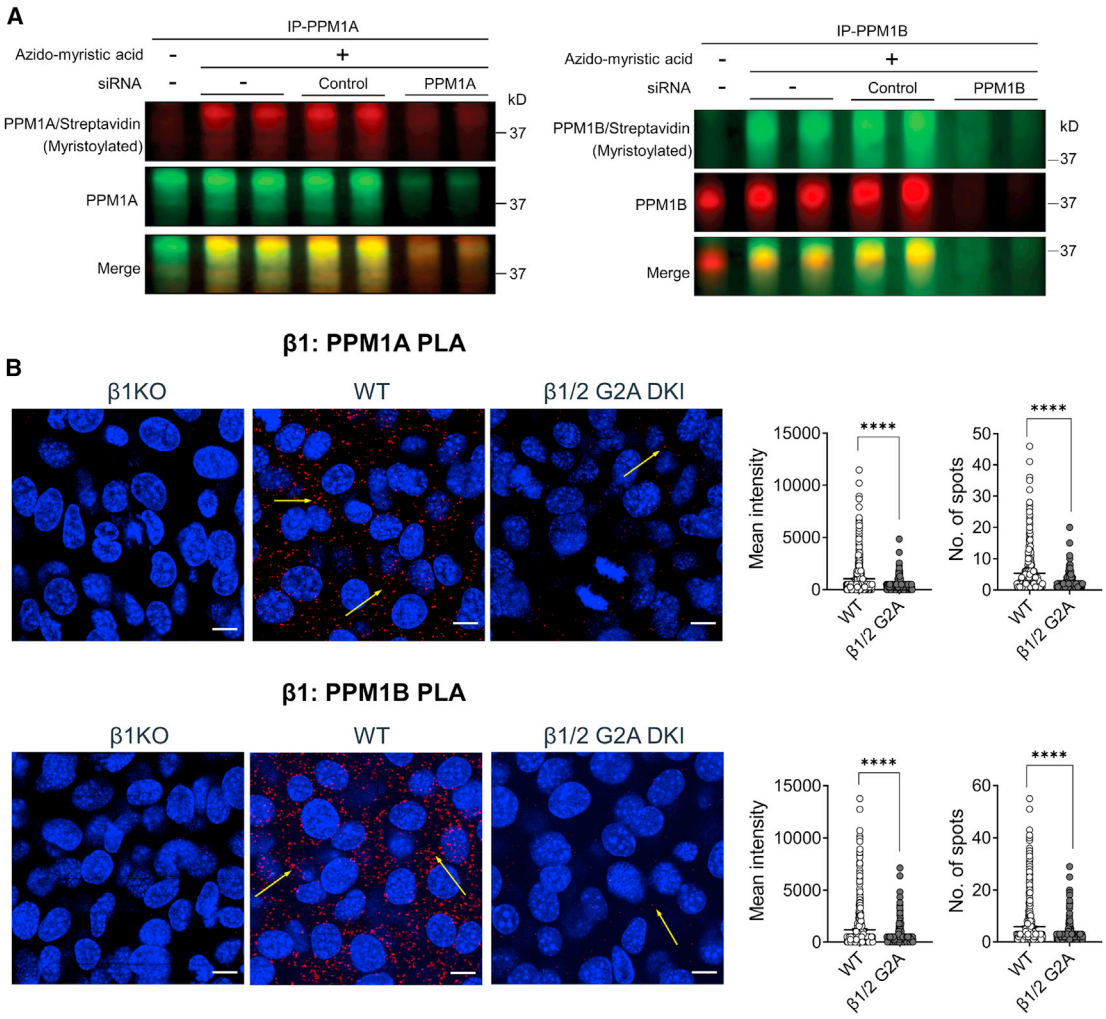

Figure 2. PPM1A and PPM1B are myristoylated and colocalize with AMPK β1 in cells

(A) WT MEFs were incubated with azido-myristic acid for 16 h. Cells were left untransfected (−) or transfected (+) with scrambled siRNA (control) or siRNA targeting PPM1A or PPM1B for 48 h. Immunoprecipitated PPM1A (left panel) or PPM1B (right panel) was subjected to a click chemistry reaction followed by immunoblot analysis. Myristoylated and total PPM1A or PPM1B were detected by streptavidin-AF680 or total PPM1A or PPM1B antibodies and visualized using the LI-COR Biosciences Odyssey Blot Imager.

(B) Colocalization of AMPK β1 and PPM1A (top panel) or PPM1B (bottom panel) was visualized by proximity ligation assay (PLA) in β1 KO, WT, or β1/2-G2A DKI MEFs. Representative images shown were from at least two independent experiments. Signal was quantified as mean fluorescence intensity (relative to WT) or number of dots per given field using ImageJ plugins. Scale bars, 10 μm. ****$p < 0.0001$ as determined by unpaired Student's t test.

All data are mean ± SEM. See also Figures S3 and S4.

expression of non-myristoylated G2A mutants of PPM1A or PPM1B was associated with blunted dephosphorylation of AMPK α-Thr172 in HeLa cells.[9] We show that ablation of AMPK myristoylation results in a significant reduction of AMPK-phosphatase interactions, possibly contributing to enhanced AMPK phosphorylation and activity.

Blocking AMPK β1 Gly2 myristoylation protects from high-fat diet-induced hepatic steatosis

To determine the effect of disrupted AMPK β1 myristoylation in an *in vivo* setting, we investigated metabolic regulation in β1-G2A KI mice with specific global blockage of AMPK β1 myristoylation. We first analyzed AMPK activity and subunit expression in the liver, a tissue reported previously to predominantly express the β1 isoform.[28,31,32] We isolated livers from male β1-G2A KI and WT littermates that were fed *ad libitum* or fasted for 16 h as a physiologically relevant means of AMPK activation. Relative tissue expression of β isoforms was determined by immunoblot using a pan-β antibody raised against an epitope that is fully conserved between the β1 and β2 isoforms (Cell Signaling Technology, 4150).[32,33] We found that, in agreement with previous findings, mouse liver predominantly expresses the β1 isoform (>93% of total β signal; Figures 3A and 3B), with the β1-G2A mutation therefore expected to have significant effects on AMPK function in this tissue.

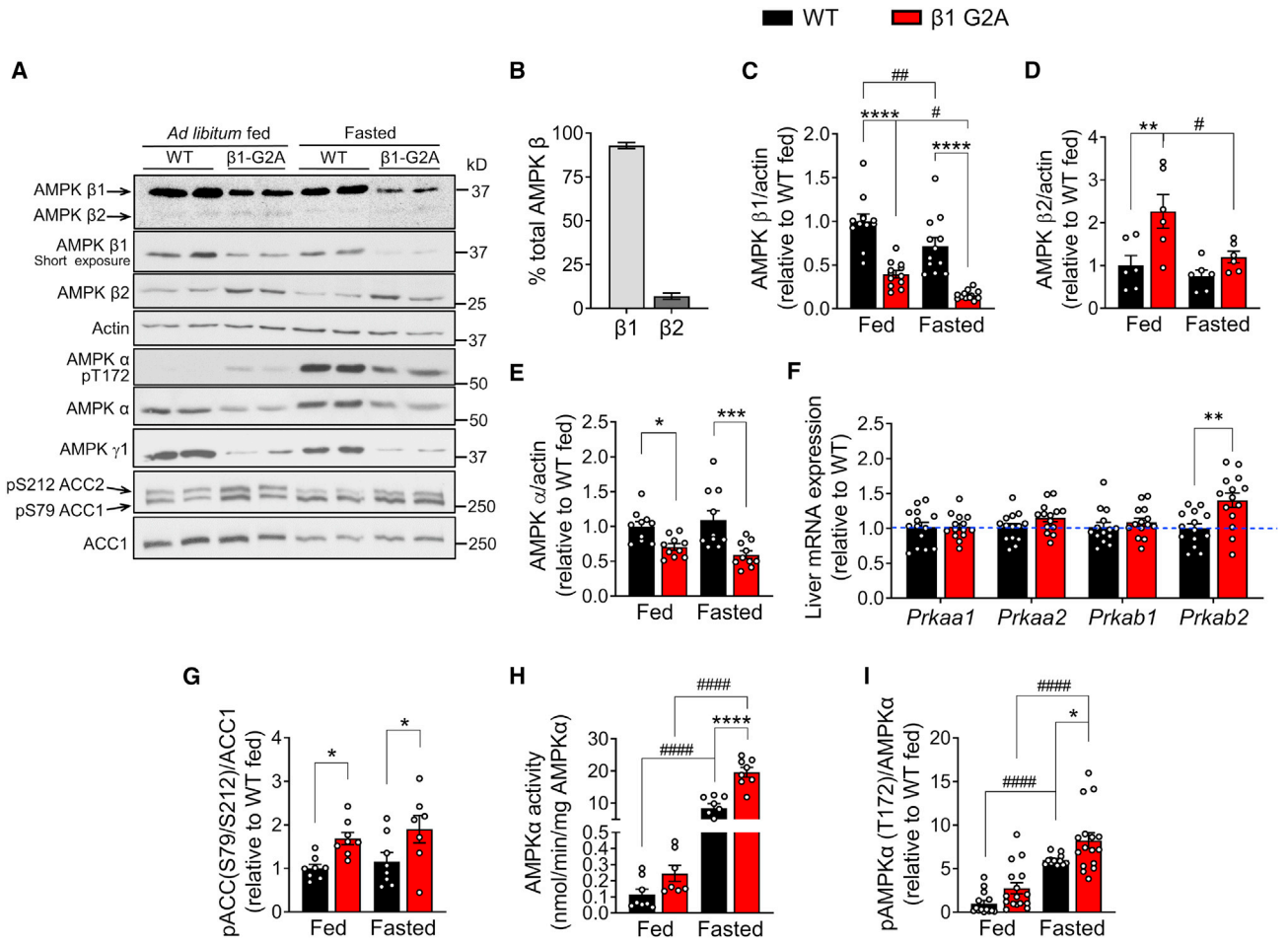

Figure 3. Ablation of AMPK β1 myristoylation increases liver AMPK activity

(A) Male age-matched 20- to 24-week-old β1-G2A and WT mice (n = 6–16) were fed *ad libitum* or fasted for 16 h, and livers were isolated for immunoblot analysis.

(B–E) Densitometry analysis of (B) AMPK β-isoform content after immunoblotting with AMPK pan-β antibody, showing expression of each β isoform as a percentage of total AMPK β, (C) AMPK β1, (D) AMPK β2, and (E) AMPK pan-α normalized to the pan-actin signal.

(F) mRNA expression analysis of AMPK α and β subunits in livers from *ad libitum*-fed mice.

(G) Densitometry analysis of ACC1/2 Ser79/Ser212 phosphorylation relative to ACC1 signal in immunoblots shown in (A) (n = 8).

(H) Kinase activity of AMPK pan-α immunoprecipitated from *ad libitum*-fed and 16-h-fasted β1-G2A and WT mice normalized for AMPK α recovered, as determined using separate immunoblots processed in parallel (n = 8).

(I) Densitometry analysis of AMPK α-Thr172 phosphorylation in immunoblots shown in (A) (n = 12–16).

*p < 0.05, **p < 0.01, ***p < 0.001, and ****p < 0.0001 represent genotype differences, and #p < 0.05, ##p < 0.01, and ####p < 0.0001 represent treatment effects, as determined by two-way ANOVA and Šídák's post hoc test. All data are mean ± SEM. See also Figures S5 and S6.

Consistent with our findings in MEFs, blocking β1 myristoylation in the liver resulted in a reduced abundance (~50%) of the β1 subunit in the fed and fasted state (Figures 3A and 3C). This was accompanied by an ~2-fold increase in β2 (Figures 3A and 3D) and a drop in total AMPK α (~40%; Figures 3A and 3E) and AMPK γ1 (~70%; Figure 3A), the predominant γ subunit in rodent liver. qPCR analyses confirmed that the increase in β2 levels was at least in part due to upregulation of *Prkab2* gene expression, whereas the reduction in β1 and α subunit abundance was independent of changes in mRNA expression (Figure 3F), indicative of increased posttranslational turnover.

Despite decreased AMPK α protein levels, livers from β1-G2A KI mice had overall elevated ACC phosphorylation (Figures 3A and 3G), reflecting increased cellular AMPK activity. To investigate this further, we measured kinase activity of AMPK complexes using AMPK α immunoprecipitated from β1-G2A KI and WT liver homogenates and accounted for the difference in AMPK abundance by normalizing activity to the amount of α subunit recovered. We found an overall genotype effect on AMPK specific activity ($p < 0.0001$) with a 2.3-fold increase in homogenates from β1-G2A mice compared with WT in the fasted state (Figure 3H). This finding correlated with an overall increase in AMPK α-Thr172 phosphorylation (genotype effect, $p = 0.027$) (Figures 3A and 3I), suggesting that β1 myristoylation *in vivo* has an inhibitory effect on Thr172 phosphorylation and AMPK activity.

Analysis of AMPK expression and signaling in other metabolically relevant tissues isolated from *ad libitum*-fed and overnight-fasted AMPK β1-G2A KI mice showed that blocking β1 myristoylation had no measurable effects on AMPK α and β subunit expression or AMPK α-Thr172 and ACC2 Ser212 phosphorylation in skeletal muscle, consistent with negligible expression levels of AMPK β1 in this tissue (<2% of total β; Figure S5A).[34] Similarly, there were no significant differences in AMPK expression and signaling in β1-G2A KI and WT hypothalami (25% β1/75% β2, Figure S5B) or subcutaneous white fat (49% β1/51% β2; Figure S6A), with WT AMPK β2 complexes likely compensating for changes in the function of the non-myristoylated β1-G2A mutant in these tissues.[35] In contrast, β1-G2A KI brown adipose tissue (84.5% β1/15.5% β2; Figure S6B) showed many of the changes in AMPK biology observed in the liver, but to a lesser degree, including reduced AMPK β1 and α subunit expression and increased ACC phosphorylation, indicative of an overall increase in AMPK activity. These results suggest that the metabolic effect of the β1-G2A mutation *in vivo* may be predominantly a consequence of altered signaling in the liver and brown adipose tissue.

Myristoylation of the AMPK β subunit has been suggested previously to be a prerequisite for AMP-induced stimulation of α-Thr172 phosphorylation.[17] To investigate the effect of the β1-G2A mutation on AMPK signaling in a system that allows greater control of intracellular AMP levels, we isolated primary hepatocytes from AMPK β1-G2A and WT mice and analyzed ACC phosphorylation as a readout of cellular AMPK activity in response to AICAR. β1-G2A hepatocytes showed significantly increased basal and similar levels of AICAR-stimulated ACC phosphorylation (Figures 4A and 4B). ACC phosphorylation was maintained for a longer period in β1-G2A cells (Figures 4A and 4B) and correlated with prolonged α-Thr172 phosphorylation (Figures 4A and 4C). A similar pattern of elevated basal and comparable maximal ACC phosphorylation was observed in hepatocytes treated with the β1-selective AMPK activator A769662[36] (Figures S7A and S7B).

To assess the consequences of increased ACC phosphorylation in β1-G2A liver for hepatic lipid accumulation *in vivo*, we analyzed fat content in liver tissue from β1-G2A mice and WT controls fed a chow or obesity-inducing high-fat diet (HFD). There was no difference in the overall area of oil red O lipid stain in livers from chow-fed AMPK β1-G2A and WT mice and no apparent morphological difference, as assessed by hematoxylin and eosin (H&E) staining (Figures S7C and S7D). However, after 12 weeks of HFD feeding, livers from β1-G2A mice had significantly smaller lipid droplets (Figures 4D and S7D) and reduced fat content, as assessed by nuclear magnetic resonance (NMR) analysis of liver biopsies (Figure S7E). Quantification of liver triglyceride content revealed decreased levels in β1-G2A livers from chow-fed (Figure 4E) and HFD-fed mice (Figure 4F) across all conditions examined. In comparison, there were only minor differences in liver glycogen content between genotypes (Figure S7F), indicating a predominant effect of the β1-G2A mutation on lipid metabolism.

To investigate whether the reduced liver lipid content in β1-G2A mice may have been indirectly affected by altered AMPK signaling and inhibited triglyceride lipolysis in adipose tissue, we assessed phosphorylation of hormone-sensitive lipase (HSL) Ser565, an AMPK phosphorylation site reported previously to have inhibitory effects on lipolysis.[37,38] We found no measurable difference in HSL Ser565 phosphorylation in subcutaneous white fat during the *ad libitum* or fasted states (Figure S7G), consistent with our previous observation that blocking AMPK β1 myristoylation had no significant effect on AMPK signaling in this tissue. To analyze whether intestinal lipid absorption was affected in β1-G2A mice, we measured serum triglyceride levels in response to an oral lipid tolerance test. AMPK β1-G2A mice and WT controls were fasted overnight, followed by gavage with Intralipid (20% soybean oil [v/v]). We found that the rise in serum triglyceride levels after lipid challenge was similar between genotypes (Figure S7H). Consistent with this, serum triglyceride levels of fasted or *ad libitum*-fed β1-G2A mice were indistinguishable from the WT across all conditions examined (Figure S7I), suggesting that the reduced hepatic fat content of β1-G2A mice was not due to reduced lipid uptake from the circulation.

We next analyzed the capacity for hepatic *de novo* triglyceride synthesis by measuring rates of ^{3}H-acetate incorporation in primary hepatocytes isolated from β1-G2A and WT mice. We found that β1-G2A cells had reduced basal and insulin-induced *de novo* triglyceride synthesis, whereas the lipid-lowering effect of A769662 was not significantly different between genotypes (Figure 4G). The decreased lipogenic capacity of β1-G2A hepatocytes was likely due to increased suppression of ACC activity and not gene expression differences because qPCR analyses of β1-G2A livers showed no change or a possibly compensatory increase in a number of lipogenic genes examined (Figure S7J). We also assessed effects on fatty acid catabolism by measuring the conversion of ^{14}C-palmitate to acid-soluble metabolites. We found a modest increase in basal oxidation rates in β1-G2A hepatocytes (Figure 4H), whereas treatment with A769662 had no significant additional effect on oxidation in G2A cells.

These results indicate that deletion of β1 myristoylation maintains AMPK in an active state, altering lipid metabolism in hepatocytes and preventing hepatic lipid accumulation during HFD feeding.

AMPK β1-G2A KI mice have reduced adiposity and improved insulin sensitivity on an HFD

To determine the effect of non-myristoylated AMPK β1 on whole-body metabolism, we monitored the body mass and adiposity of male β1-G2A mice and age-matched WT controls fed a chow or HFD over a period of 12 weeks. There was no significant difference in body weight progression in chow-fed mice, but β1-G2A mice were partially protected from body weight gain during HFD feeding (Figure 5A). This was not attributable to differences in lean mass (Figure 5B) but instead due to a significant reduction in total body fat mass, which was, to a smaller degree, also detectable in chow-fed animals (Figure 5C). Epididymal visceral fat pads dissected from age-matched β1-G2A mice and WT littermates at the end of the 12-week feeding period were significantly smaller in β1-G2A animals under chow- and HFD-fed conditions (Figure 5D). The reduced adiposity of HFD-fed β1-G2A mice was of potential therapeutic significance because it was associated with increased glucose clearance after insulin

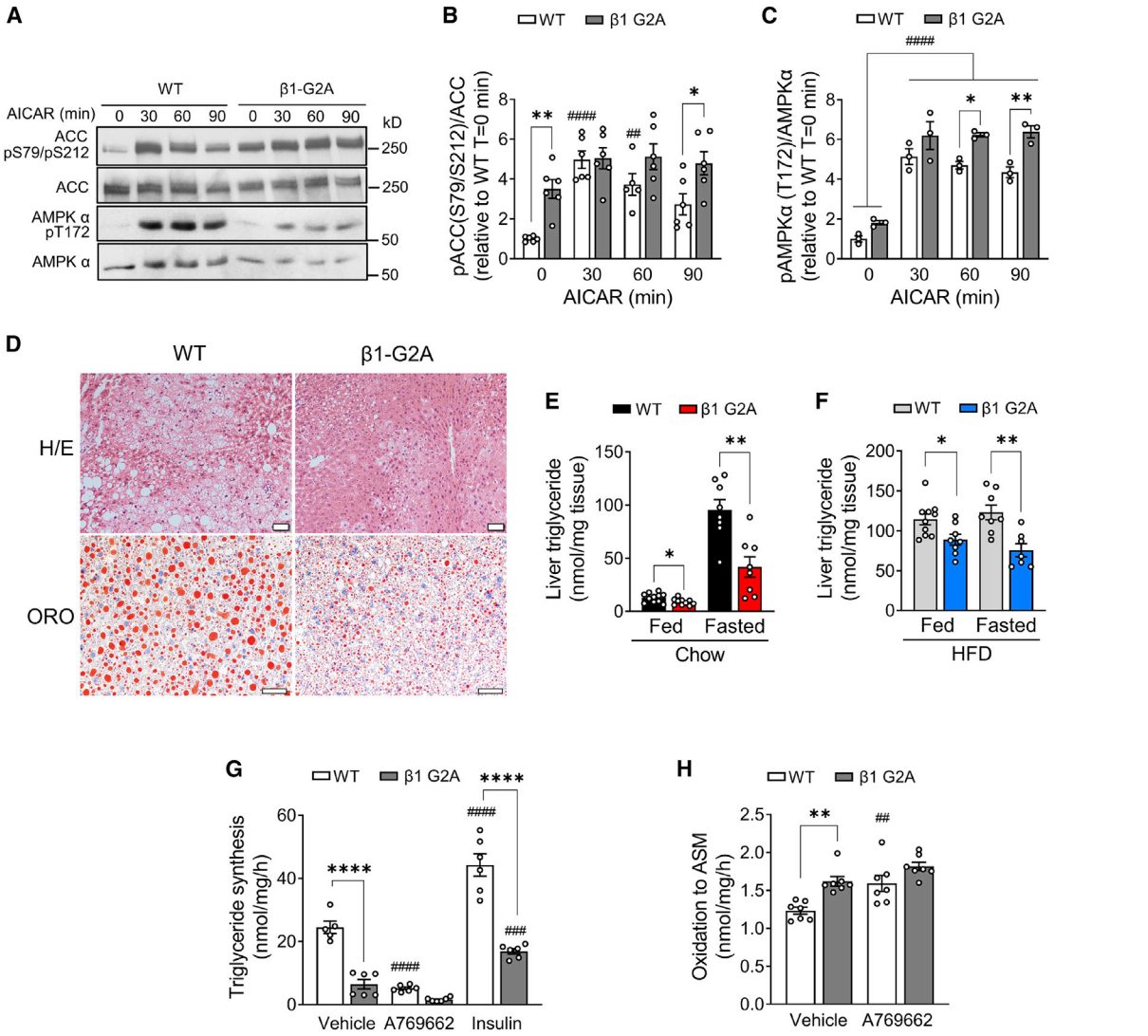

Figure 4. Ablation of AMPK β1 myristoylation protects from HFD-induced hepatic steatosis

(A) Time course of ACC1/2 Ser79/Ser212 and AMPK α-Thr172 phosphorylation in response to 0.25 mM AICAR in primary hepatocytes isolated from β1-G2A and WT mice. Total ACC was detected by enhanced chemiluminescence using streptavidin-horseradish peroxidase (HRP). Shown are representative immunoblots from 3–6 hepatocyte preparations.

(B and C) Densitometry analysis of (B) ACC1/2 Ser79/Ser212 phosphorylation of the immunoblot shown in (A), normalized to streptavidin-HRP signal (n = 6), and (C) AMPK α-Thr172 phosphorylation, normalized to AMPK pan-α signal (n = 3), treated with 0.25 mM AICAR.

(D) Hematoxylin and eosin (H&E; top panel) and oil red O (ORO; bottom panel) staining of *ad libitum*-fed β1-G2A mice and WT littermate controls fed a high-fat diet (HFD). Shown are representative images from 6 mice per condition. Scale bars, 50 μm.

(E and F) Triglyceride content in liver tissue from *ad libitum*-fed and 16-h-fasted β1-G2A and WT mice on (E) chow (n = 8–11) and (F) HFD (n = 7–10).

(G and H) Triglyceride synthesis (G, n = 6) and oxidation rates of [^{14}C]-palmitic acid to acid-soluble metabolites (H, n = 7) in β1-G2A and WT primary hepatocytes. *p < 0.05, **p < 0.01, and ****p < 0.0001 represent genotype differences, and ##p < 0.01, ###p < 0.001, and ####p < 0.0001 represent treatment effects, as determined by two-way ANOVA and Šídák's post hoc test or unpaired Student's t test (E and F). All data are mean ± SEM. See also Figure S7.

injection (Figure 5E). In contrast, glucose tolerance was indistinguishable between genotypes (Figure 5F). Consistent with this, blood glucose levels were similar in β1-G2A and WT mice (Figure 5G) but maintained on the background of significantly lower serum insulin concentrations in β1-G2A animals (Figure 5H), suggesting improvements in insulin sensitivity, a notion also supported by a significantly lower HOMA IR (Figure 5I). In contrast, there was no effect of genotype in blood glucose handling in response to insulin (Figure S8A) or glucose (Figure S8B) in chow-fed animals. Accordingly, serum insulin (Figure S8C) and blood glucose (Figure S8D) concentrations in the fed and fasted states were similar in β1-G2A and WT mice.

Histological analysis of subcutaneous adipose tissue revealed a shift to significantly smaller lipid droplets in adipocytes from inguinal subcutaneous adipose tissue from β1-G2A animals under chow- and HFD-fed conditions (Figure 6A). To investigate whether

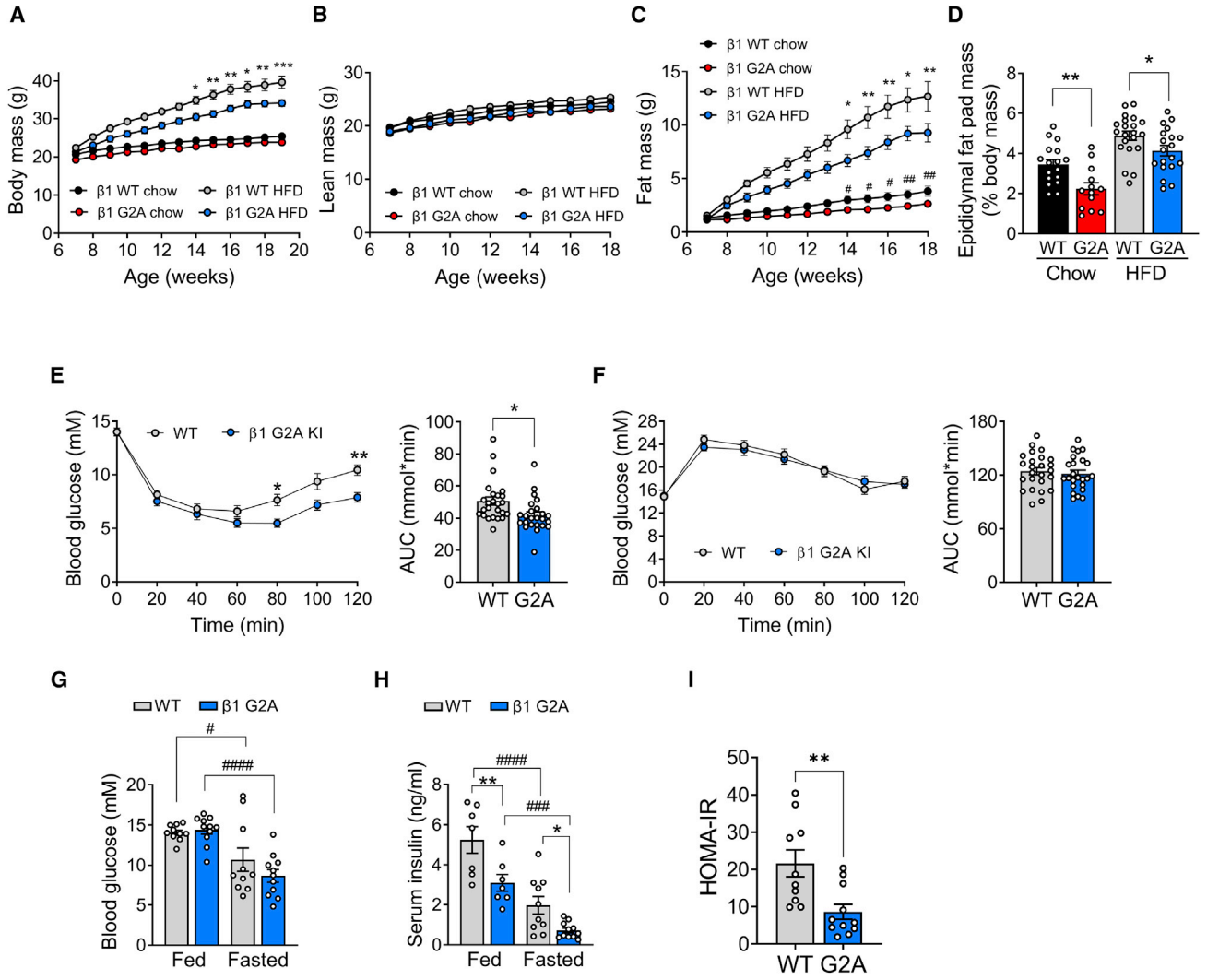

Figure 5. AMPK β1-G2A mice show reduced adiposity and improved insulin sensitivity with high-fat feeding

Male AMPK β1-G2A and WT mice were fed a chow (n = 24–28) or HFD (n = 10–11) from 6 weeks of age, and body mass and body composition were measured weekly for 12–13 weeks.

(A) Weekly body mass progression.

(B and C) Weekly lean mass (B) and weekly fat mass (C) as determined by NMR.

(D) Epididymal fat pad mass relative to total body mass at 19–22-weeks of age (n = 13–17 chow, n = 19–21 HFD).

(E) HFD-fed AMPK β1-G2A and WT mice (n = 24–25, 12 weeks of age) were fasted for 4 h and subjected to an intraperitoneal insulin tolerance test (1.2 U/kg lean mass), and the area under the curve (AUC) was analyzed.

(F) Intraperitoneal glucose tolerance test (1 g D-glucose/kg lean mass) of HFD-fed AMPK β1-G2A and WT mice (n = 24–25, 13 weeks of age) fasted for 6 h, with AUC shown.

(G and H) Blood glucose (G, n = 10–11) and serum insulin (H, n = 7–11) concentrations of *ad libitum*-fed and 16-h-fasted 19- to 20-week-old β1-G2A mice and WT littermates on the HFD.

(I) HOMA IR calculated from 16-h-fasted glucose and insulin levels (n = 10–11).

*p < 0.05 and **p < 0.01 represent genotype differences. #p < 0.05, ###p < 0.001, and ####p < 0.0001 represent treatment differences. Analyses of progression of body mass and body composition (A–C) were performed using repeated-measures two-way ANOVA with Šídák's post hoc test. All other analyses were performed by ordinary two-way ANOVA and Šídák's post hoc test (G and H) or unpaired Student's t test (AUC and D and I). All data are mean ± SEM. See also Figure S8.

browning of subcutaneous fat deposits contributed to the lean phenotype of β1-G2A mice, we performed immunohistochemical analysis of UCP1 expression in inguinal fat tissue of chow- and HFD-fed β1-G2A and WT mice. We did not observe any detectable UCP1-associated signal in any of the tissue sections examined (Figure S9A). Similarly, immunoblot analysis revealed only a spurious UCP1 signal in tissues from chow-fed or HFD-fed animals independent of genotype (Figure S9B), suggesting that that loss of β1 myristoylation does not result in increased thermogenic capacity in subcutaneous tissue. A recent study using mice with

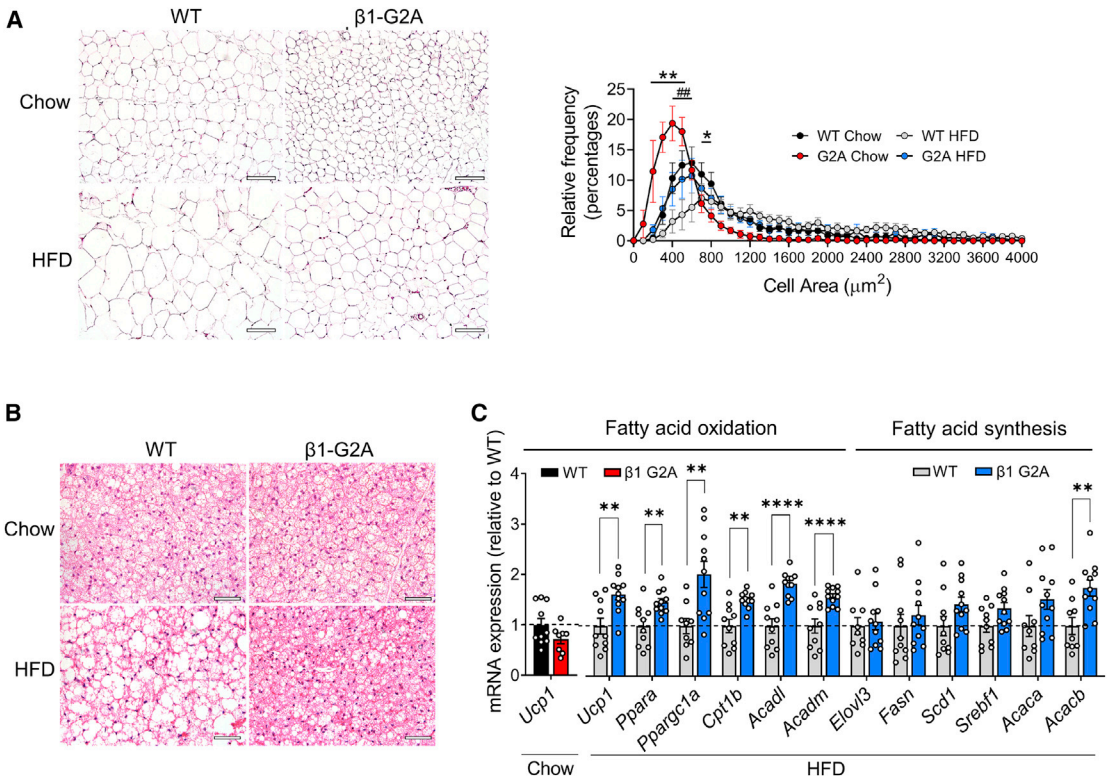

Figure 6. AMPK β1-G2A mice have reduced adipose tissue fat cell size and show adaptations for increased brown fat lipid catabolism on an HFD

(A) H&E-stained inguinal subcutaneous adipose tissue sections from chow (20- to 24-week-old) and HFD-fed (19- to 22-week-old) β1-G2A and WT mice. Representative sections from 6 mice per condition and genotype are shown. Scale bars, 100 μm. The graph shows frequency distribution of the average adipocyte area as analyzed from 3–4 representative images from 6 mice per condition and genotype. To enhance clarity, distributions of cells with an area greater than 4,000 μm^2 were omitted from the graph. Distribution was calculated by GraphPad Prism software, and differences within each area bin were analyzed by multiple t tests and corrected for multiple comparisons using the Holm-Šídák method. *$p < 0.05$ and **$p < 0.01$ represent differences between genotypes on chow diet; ##$p < 0.01$ represents differences between genotypes on the HFD.

(B) H&E staining of interscapular brown adipose tissue sections from chow (20- to 24-week-old) and HFD-fed (19- to 22-week-old) β1-G2A and WT mice. Representative sections from 6 mice per condition and genotype are shown. Scale bars, 50 μm.

(C) mRNA expression analysis of *Ucp1* in brown adipose tissue of 20- to 24-week-old chow-fed (n = 8–10) and *Ucp1* and genes involved in fatty acid oxidation or fatty acid synthesis in 19- to 22-week-old HFD-fed (n = 10–11) β1-G2A and WT mice. **$p < 0.01$, ***$p < 0.001$, and ****$p < 0.0001$ represent genotype differences as analyzed by unpaired Student's t test.

All data are mean ± SEM. See also Figures S9–S11.

widespread expression of a gain-of-function AMPK mutant (γ1-D316A) showed that chronic global AMPK activation protects from diet-induced obesity, likely by promoting a UCP1-independent increase in the oxygen consumption rate in white adipose tissue because of increased mitochondrial content and expression of skeletal muscle-associated genes.[39] To assess whether a similar mechanism may contribute to the obesity-resistant phenotype of β1-G2A mice, we analyzed the mRNA expression of genes involved in UCP1-independent thermogenesis in inguinal fat from HFD-fed β1-G2A and WT mice. There were no significant differences in the transcription of any of the genes examined (Figure S9C). Similarly, protein levels of mitochondrial electron-transport-chain proteins in inguinal fat of chow- and HFD-fed mice were comparable between genotypes (Figure S9D). These results suggest that the reduced adiposity of β1-G2A mice is independent of functional changes within white adipose tissue, consistent with overall unaltered AMPK signaling in this tissue (Figure S6A).

We have shown that, in addition to effects in the liver, non-myristoylated AMPK β1 also had measurable effects on ACC1/2 Ser79/Ser212 phosphorylation in brown fat, indicative of increased overall AMPK activity. AMPK has been found previously to be crucial for maintaining UCP1 expression and thermogenesis in brown fat depots,[40] suggesting that the reduced adiposity of HFD-fed β1-G2A may have been due to increased brown fat activity. H&E staining of brown fat tissue sections showed smaller adipocyte size and reduced fat content in tissue isolated from HFD-fed β1-G2A animals compared with WT controls (Figure 6B). Analysis of *Ucp1* mRNA levels in brown fat revealed no difference in expression in tissue from chow-fed animals, but HFD-fed β1-G2A mice showed a modest increase in *Ucp1* expression, indicating a possible increase in thermogenic capacity (Figure 6C). mRNA expression analysis of several other genes involved in brown fat lipid metabolism confirmed an increased adaptation to fatty acid

utilization versus synthesis in brown fat of HFD-fed β1-G2A mice (Figure 6C).

To investigate whether the changes in the brown fat gene expression pattern in HFD-fed mice were associated with differences in whole-body energy expenditure, we performed calorimetry analysis using the Columbus Laboratory Animal Monitoring System (CLAMS) over a period of 48 h. We found that non-myristoylated AMPK β1 had no statistically significant effect on energy expenditure (Figures S10A and S10B). To account for any potential confounding effects stemming from differences in adiposity, we performed regression analysis of the average rate of energy expended over a 24-h period per unit change in total body mass or lean mass (Figure S10C), including analysis of covariance (ANCOVA) of the mean difference in energy expenditure in a given time period, with total body mass or lean mass as covariates (Figure S10D). The analyses showed the expected effect of diet and mass on metabolic rate without revealing any significant genotype differences, suggesting that any potentially activating effect of non-myristoylated β1 on thermogenesis did not translate into any overt effects on whole-body energy expenditure measured over a 48-h period. Ambulatory activity (Figures S10E and S10F), substrate preference (as determined by the respiratory exchange ratio, defined as the ratio of the volume of CO_2 produced and volume of O_2 consumed [VCO_2/VO_2]) (Figures S10G and S10H), and average 24-h cumulative food intake measured in CLAMS (Figures S10I and S10J) or in the familiar home cage environment (Figure S10K) were also unaffected by the β1-G2A mutation. To assess effects on appetite in response to AMPK-activating conditions, we measured food consumed within 2 h after an overnight fast but did not detect any differences between genotypes (Figure S11A). Consistent with this, fasting-induced c-Fos activation in the arcuate nucleus (Figure S11B) and ventromedial hypothalamus (Figure S11C), as a readout of neuronal activity in hypothalamic structures associated with appetite regulation, was indistinguishable in HFD-fed WT and β1-G2A KI mice.

Overall, these results suggest that the reduced adiposity of β1-G2A mice is independent of energy intake, activity levels, or functional changes within white adipose tissue but possibly a consequence of small increases in brown fat thermogenic capacity accumulated over a period of long-term HFD feeding combined with extrahepatic benefits of liver-specific AMPK activation.[41]

DISCUSSION

In this study, we described the role of AMPK β1-Gly2 myristoylation in regulation of AMPK signaling and whole-body energy metabolism. In contrast to previous studies, which have almost exclusively relied on cellular overexpression methods to investigate AMPK β-myristoyl group function, we utilized a CRISPR-Cas9-generated Gly2-to-Ala KI system, which enabled us to block myristoylation of the endogenous AMPK β1 protein.

We found that ablation of Gly2 myristoylation resulted in decreased abundance of the β1 subunit protein independent of changes in mRNA expression. It is possible that mutation of the codon required for Gly-to-Ala substitution (positions +4 to +6 from the starting AUG of the *Prkab1* mRNA) may have sufficiently altered the Kozak context to affect initiation of β1-G2A protein synthesis. However, it has been reported that mutations in position +5, as in our case (GGC to GAC), should have minimal effects on start codon recognition and are therefore unlikely to affect translation of the mutant *Prkab1* mRNA.[42] Another explanation for the decreased G2A protein abundance may be enhanced proteasomal degradation. Because of its N-terminal position, substitution of Gly-2 may destabilize the resultant mutant protein by making it a better target for the N-end rule pathway of the ubiquitination system.[43] Consistent with this, myristoylation of N-terminal glycines functions to protect proteins from degradation by Cullin-RING E3 ligase complexes, $Cul2^{ZYG11B}$, and $Cul2^{ZER1}$ of the Arg/N-end rule pathway.[44] However, substitution of Gly-2 for Ala has also been reported to enhance protein stability in this context,[44] suggesting that other ubiquitin systems may contribute to increased degradation of the β1-G2A protein. Examples are the E3 ligases cell death-inducing DFFA-like effector A (CIDEA), RING finger protein 44 (RNF44), ubiquitin-conjugating enzyme E2O (UBE2O) and Cereblon (CRBN), which have all been suggested to promote β subunit degradation.[45,46] Alternatively, as occurs for the majority of cellular proteins, the N-terminal Ala of the G2A mutant, upon removal of the initiator methionine, may present a target for N-acetyltransferases, with the N-acetylated product subsequently recognized for Ac/N-end rule pathway ubiquitination.[47,48] Two E3 ubiquitin ligases, the yeast protein Doa10 (MARCH6/TEB4 in mammals) and Not4, have been implicated in mediating degradation of such N-acetylated proteins.[47,49] Future studies may clarify whether a similar mechanism is responsible for the reduced abundance of β1-G2A in our system.

Despite reduced total cellular levels of AMPK complex components, basal phosphorylation of all AMPK substrates examined was significantly increased in cells expressing non-myristoylated (G2A) AMPK β1 and correlated with increased basal α-Thr172 phosphorylation and AMPK activity. Previous studies using purified AMPK complexes *in vitro*[17,18] have reported that loss of β myristoylation results in enhanced AMPK activation under the basal condition. The increase in kinase activity has been found to be at least in part independent of α-Thr172 phosphorylation and suggested to be a consequence of altered subunit interactions in the absence of the myristoyl group.[18] The structural basis for the increased activity is not entirely clear but may involve disruption of the normal functioning of a "myristoyl switch" mechanism, by which the myristoyl group is normally buried in a putative hydrophobic binding pocket (switch OFF) and moves out in response to activating conditions enabling AMPK to interact with membrane associated proteins (switch ON) (Figure 1A).[17,50] It is possible that non-myristoylated AMPK mimics a perpetual "switch ON" conformation that alleviates AMPK autoinhibition even in the absence of activating conditions. In support of this, we previously reported an interaction between a short, β1-conserved sequence in the N-terminal region of the β2 isoform and the α2 autoinhibitory domain in the disengaged position, itself associated with higher basal AMPK activity and resistance to Thr172 dephosphorylation.[51] Clearly, more detailed structural studies, ideally interrogating myristoylated AMPK complexes, are required to understand the precise mechanism.

An additional aspect of AMPK myristoyl group function is targeting of AMPK to subcellular membranes in response to activating stimuli. Multiple studies overexpressing fluorescently tagged AMPK β G2A protein have shown the importance of the myristoyl group for targeting of AMPK to subcellular structures[17,18,23–25] and into the vicinity of upstream kinases (LKB1[24] and ULK1[26]) and downstream signaling proteins (Raptor/mTORC1[23] and ATG16 complex[25]). However, overexpression methods may introduce artifacts[52] that result in mislocalization of the tagged protein. Using immunofluorescence analysis of natively expressed non-myristoylated protein, we detected a modest inhibitory effect of the G2A mutation on fluorescence co-occurrence between AMPK β1 and the lysosomal marker LAMP1, indicating that β1 subunit myristoylation may indeed facilitate intracellular membrane targeting of endogenous AMPK complexes. Such a reduction in membrane localization and, presumably, reduced targeting to the lysosome-associated kinase LKB1 would be expected to correlate with inhibited AMP-induced AMPK signaling and activation.[17,24] However, AMPK phosphorylation and signaling were consistently elevated in cells and tissues expressing high levels of the β1 G2A mutant, suggesting that membrane targeting is not a requirement for effective AMPK activation. It is possible that β subunit myristoylation may primarily serve other functions, such as the abovementioned protection from ubiquitin-mediated degradation or the targeting to other lipidated molecules for signal complex formation.

In agreement with this, our current data suggest that the AMPK myristoyl group may provide a separate layer of regulation of AMPK activity by facilitating spatial targeting of myristoylated α-Thr172 phosphatases to AMPK for effective deactivation. Basal phosphorylation of α-Thr172 and AMPK substrates in G2A cells was close to saturating levels because treatments with various AMPK activators had only modest effects or were entirely ineffective at eliciting further increases. Time course analyses of AICAR-stimulated hepatocytes showed a pattern of prolonged phosphorylation of α-Thr172 and ACC Ser79, indicating a delay in deactivation of the non-myristoylated mutant. In cell-free assays, AMPK α-Thr172 has been shown to be dephosphorylated by recombinant/purified protein phosphatases, including PP1, PP2A, and PPM1A.[10,53] In cellular studies, RNAi-mediated knockdown of PPM1A/B or PPM1E resulted in reduced dephosphorylation of AMPK α.[9,54] Chida et al.[9] demonstrated that ectopically/stably expressed PPM1A/B Gly-2 are myristoylated in HeLa cells and that the overexpressed WT PPM1A/B, but not the G2A mutant, caused a large decrease in AMPK α phosphorylation. We extended this observation and showed here that endogenous PPM1A/B are myristoylated in cells and that they are in close proximity with endogenous AMPK β1 WT but to a significantly lower extent with the G2A mutant. These results suggest that myristoylation of PPM1A/B and AMPK β may promote their colocalization and at least partly contribute to keeping AMPK α-Thr172 phosphorylation at a low level in cells.

At the whole-body level, the increased AMPK α-Thr172 phosphorylation and kinase activity of the non-myristoylated mutant had profound effects on adiposity and liver lipid metabolism, reminiscent of the previously described phenotype of a whole-body gain-of-function γ1-D316A transgenic mouse model.[39] However, in contrast to the γ1-D316A mutation, which affects AMPK β1 and β2 complexes, study of the AMPK G2A mutation enabled us to determine the metabolic consequences of β1-specific AMPK activation. We found that loss of β1 myristoylation was sufficient to afford partial protection from HFD-induced obesity with reduced lipid accumulation across all fat depots examined. In contrast to the phenotype of γ1-D316A transgenic mice, which displayed increased oxygen consumption associated with a dramatic induction of a skeletal muscle gene signature in subcutaneous fat,[39] ablation of β1 myristoylation had no measurable effects on thermogenic, mitochondrial, or muscle-like protein and gene expression in white fat tissue. This was likely due to compensatory effects of β2-WT, which, as we have shown, constitutes up to 50% of AMPK complexes in this tissue. Future studies using mice with ablation of β1- and β2-specific Gly-2 myristoylation may clarify whether AMPK activation through lack of myristoylation has the potential to remodel adipose tissue function.

In contrast, β1 is the principal AMPK β subunit in mouse liver. Consistent with this, β1-G2A mice showed substantial reductions in liver fat accumulation, particularly under conditions of an HFD, which were likely due to increased ACC inhibition leading to reduced lipid synthesis and modest increases in fatty acid oxidation. This finding is entirely consistent with numerous previous mouse models of whole-body or liver-specific AMPK activation[39,41,55] and confirms that AMPK activation in the liver is a viable strategy for prevention of HFD-induced hepatic steatosis.

In addition to the anti-steatotic effect in the liver, ablation of AMPK β1 myristoylation also resulted in reduced lipid deposition in white and brown adipose tissue depots, suggesting that β1-G2A mice were suffering from an overall negative energy balance. Our analysis of AMPK subunit expression and signaling in metabolically relevant tissues revealed a potential role of myristoylated AMPK β1 in brown fat, in accordance with our previous report showing predominant expression of the β1 subunit in this tissue type.[56] AMPK is known to be required for effective brown fat thermogenesis by maintaining mitochondrial integrity and function[40] and possibly by promoting upregulation of thermogenic genes.[57] Consistent with this, we found elevated expression of UCP1 and genes involved in fat catabolism in brown fat of HFD-fed β1-G2A mice. However, these changes did not correlate with significant effects on whole-body energy expenditure, suggesting that AMPK activation associated with loss of myristoylation in brown fat did not elicit increases in heat dissipation sufficient to affect energy balance. It is possible that the effects of small increases in brown fat activity may become apparent when accumulated over a longer time period. Alternatively, the reduced adiposity of HFD-fed β1-G2A mice may have been a consequence of altered AMPK biology in the liver. Previous studies have reported significant extra-hepatic benefits, including reduced white adipose tissue expansion, associated with liver-specific AMPK activation.[41,58] AMPK activation has been shown to alter the expression profile of the liver secretome, possibly affecting hepatokines capable of modifying whole-body metabolism.[41] Future studies may reveal whether a similar mechanism contributes to the reduced adiposity of β1-G2A mice.

Loss of AMPK β1 myristoylation produces a phenotype characterized by increased basal AMPK Thr172 phosphorylation and

activity, an effect that may at least partially be due to inhibited interactions with AMPK phosphatases. *In vivo*, these effects produce an overall metabolically beneficial outcome by combining lowered hepatic lipid accumulation with reduced HFD-induced increases in adiposity, leading to improvements in insulin sensitivity.

Limitations of the study

Our analyses of AMPK activity and signaling were performed in cells and tissues with varying levels of β2-WT expression that likely compensate for the changes induced by the non-myristoylated β1 protein. Although these conditions may be physiologically relevant, our data generated in these systems do not reveal the true extent of the activating effect of the G2A mutation on AMPK function. Use of AMPK β1/2 double KO cells reconstituted with AMPK β1-G2A versus β1-WT may prove a more suitable cell model to address this limitation.

Conclusions drawn from our immunofluorescence analysis of AMPK β1 colocalization with lysosomal membranes (Figure S4A) should be made with caution, given the reliance on the target specificity of primary and secondary antibodies used in the experiment. Although we were able to validate the specificity of the AMPK β1 antibody using β1 KO cells, we are unable to draw firm conclusions about the extent to which the signal provided by the LAMP1 antibody represents the lysosomal membrane. Furthermore, given that AMPK residency at the lysosomes is highly transient,[22] it is likely that our experimental system lacks the sensitivity required to accurately capture the dynamic process of AMPK membrane localization.

Regarding our *in vivo* data, because of restraints imposed by the necessity to ensure a sufficient number of females for colony maintenance, we restricted our study to male mice only. We are therefore unable to draw conclusions about the effect of AMPK β1 myristoylation in a female cohort. We were unable to identify the mechanism for reduced adiposity in male HFD-fed AMPK β1-G2A mice. Although we did not detect significant differences in appetite or energy expenditure, future, more detailed analyses of energy balance, including responses to specific nutritional conditions or metabolic hormones, may reveal further insight into the mechanism of the anti-obesity effect.

STAR★METHODS

Detailed methods are provided in the online version of this paper and include the following:

SUPPLEMENTAL INFORMATION

Supplemental information can be found online at https://doi.org/10.1016/j.celrep.2022.111862.

ACKNOWLEDGMENTS

This work was supported by grants from the Australian Research Council (DP170101196), the National Health and Medical Research Council of Australia (1085460 to B.E.K., S.G., and G.R.S.; 1145836 to S.G., K.L., G.R.S., and B.E.K.; and 1145265 to J.S.O. and B.E.K.) and supported in part by the Victorian Government Operational Infrastructure Support Scheme. G.R.S. is supported by a Tier 1 Canada Research Chair and a J. Bruce Duncan Endowed Chair in Metabolic Diseases. The Novo Nordisk Foundation Center for Basic Metabolic Research is an independent research center based at the University of Copenhagen, Denmark, and partially funded by an unconditional donation from the Novo Nordisk Foundation (NNF18CC0034900). We acknowledge the Core Facility for Integrated Microscopy, Faculty of Health and Medical Sciences, University of Copenhagen.

AUTHOR CONTRIBUTIONS

Conceptualization, B.E.K., K.S., and S.G.; methodology, K.S., S.G., K.L., and R.B.; investigation, K.N., N.K., L.M.-S., A.H., L.M.M., D.Y., N.X.Y.L., F.N., A.J.O., and S.G.; formal analysis, K.N., N.K., L.M.-S., A.H., D.Y., A.J.O., G.T., J.W.S., K.S., and S.G.; funding acquisition, S.G., K.S., G.R.S., J.S.O., and B.E.K.; supervision, K.S., M.J.S., S.G., K.L., and J.S.O.; writing – original draft, K.S. and S.G.; writing – review & editing, K.N., F.N., A.H., M.J.S., A.J.O., G.T., J.S.O., J.W.S., G.R.S., K.L., B.E.K., K.S., and S.G.

DECLARATION OF INTERESTS

K.N. and M.J.S. are employees of Société des Produits Nestlé (Switzerland). G.R.S. has received consulting/speaking fees from Astra Zeneca, Boehringer-Ingelheim, Cambrian BioPharma, EchoR1, Eli-Lilly, Esperion, Fibrocor Therapeutics, Merck, Novo Nordisk, Pfizer, and Poxel Pharmaceuticals; receives research funding from Esperion Therapeutics, Espervita Therapeutics, Nestle, Novo Nordisk, and Poxel Pharmaceuticals; and is co-founder and shareholder of Espervita Therapeutics.

INCLUSION AND DIVERSITY

We support inclusive, diverse, and equitable conduct of research.

Received: March 11, 2022
Revised: October 7, 2022
Accepted: November 30, 2022
Published: December 20, 2022

REFERENCES

1. Hardie, D.G., Ross, F.A., and Hawley, S.A. (2012). AMPK: a nutrient and energy sensor that maintains energy homeostasis. Nat. Rev. Mol. Cell Biol. *13*, 251–262. https://doi.org/10.1038/nrm3311.
2. Carling, D., Zammit, V.A., and Hardie, D.G. (1987). A common bicyclic protein kinase cascade inactivates the regulatory enzymes of fatty acid and cholesterol biosynthesis. FEBS Lett. *223*, 217–222. https://doi.org/10.1016/0014-5793(87)80292-2.
3. Sim, A.T., and Hardie, D.G. (1988). The low activity of acetyl-CoA carboxylase in basal and glucagon-stimulated hepatocytes is due to phosphorylation by the AMP-activated protein kinase and not cyclic AMP-dependent protein kinase. FEBS Lett. *233*, 294–298. https://doi.org/10.1016/0014-5793(88)80445-9.
4. Gluais-Dagorn, P., Foretz, M., Steinberg, G.R., Batchuluun, B., Zawistowska-Deniziak, A., Lambooij, J.M., Guigas, B., Carling, D., Monternier, P.A., Moller, D.E., et al. (2022). Direct AMPK activation corrects NASH in rodents through metabolic effects and direct action on inflammation and fibrogenesis. Hepatol. Commun. *6*, 101–119. https://doi.org/10.1002/hep4.1799.
5. Narkar, V.A., Downes, M., Yu, R.T., Embler, E., Wang, Y.X., Banayo, E., Mihaylova, M.M., Nelson, M.C., Zou, Y., Juguilon, H., et al. (2008). AMPK and PPARdelta agonists are exercise mimetics. Cell *134*, 405–415. https://doi.org/10.1016/j.cell.2008.06.051.
6. Smith, B.K., Marcinko, K., Desjardins, E.M., Lally, J.S., Ford, R.J., and Steinberg, G.R. (2016). Treatment of nonalcoholic fatty liver disease: role of AMPK. Am. J. Physiol. Endocrinol. Metab. *311*, E730–E740. https://doi.org/10.1152/ajpendo.00225.2016.
7. Hardie, D.G. (2011). AMP-activated protein kinase: an energy sensor that regulates all aspects of cell function. Genes Dev. *25*, 1895–1908. https://doi.org/10.1101/gad.17420111.
8. Steinberg, G.R., and Kemp, B.E. (2009). AMPK in health and disease. Physiol. Rev. *89*, 1025–1078. https://doi.org/10.1152/physrev.00011.2008.
9. Chida, T., Ando, M., Matsuki, T., Masu, Y., Nagaura, Y., Takano-Yamamoto, T., Tamura, S., and Kobayashi, T. (2013). N-Myristoylation is essential for protein phosphatases PPM1A and PPM1B to dephosphorylate their physiological substrates in cells. Biochem. J. *449*, 741–749. https://doi.org/10.1042/BJ20121201.
10. Davies, S.P., Helps, N.R., Cohen, P.T., and Hardie, D.G. (1995). 5'-AMP inhibits dephosphorylation, as well as promoting phosphorylation, of the AMP-activated protein kinase Studies using bacterially expressed human protein phosphatase-2C alpha and native bovine protein phosphatase-2AC. FEBS Lett. *377*, 421–425. https://doi.org/10.1016/0014-5793(95)01368-7.
11. Sanders, M.J., Grondin, P.O., Hegarty, B.D., Snowden, M.A., and Carling, D. (2007). Investigating the mechanism for AMP activation of the AMP-activated protein kinase cascade. Biochem. J. *403*, 139–148. https://doi.org/10.1042/BJ20061520.
12. Steinberg, G.R., Michell, B.J., van Denderen, B.J.W., Watt, M.J., Carey, A.L., Fam, B.C., Andrikopoulos, S., Proietto, J., Görgün, C.Z., Carling, D., et al. (2006). Tumor necrosis factor alpha-induced skeletal muscle insulin resistance involves suppression of AMP-kinase signaling. Cell Metab. *4*, 465–474. https://doi.org/10.1016/j.cmet.2006.11.005.
13. Xiao, B., Sanders, M.J., Underwood, E., Heath, R., Mayer, F.V., Carmena, D., Jing, C., Walker, P.A., Eccleston, J.F., Haire, L.F., et al. (2011). Structure of mammalian AMPK and its regulation by ADP. Nature *472*, 230–233. https://doi.org/10.1038/nature09932.
14. Hoffman, N.J., Whitfield, J., Janzen, N.R., Belhaj, M.R., Galic, S., Murray-Segal, L., Smiles, W.J., Ling, N.X.Y., Dite, T.A., Scott, J.W., et al. (2020). Genetic loss of AMPK-glycogen binding destabilises AMPK and disrupts metabolism. Mol. Metab. *41*, 101048. https://doi.org/10.1016/j.molmet.2020.101048.
15. Polekhina, G., Gupta, A., Michell, B.J., van Denderen, B., Murthy, S., Feil, S.C., Jennings, I.G., Campbell, D.J., Witters, L.A., Parker, M.W., et al. (2003). AMPK beta subunit targets metabolic stress sensing to glycogen. Curr. Biol. *13*, 867–871. https://doi.org/10.1016/s0960-9822(03)00292-6.
16. Mitchelhill, K.I., Michell, B.J., House, C.M., Stapleton, D., Dyck, J., Gamble, J., Ullrich, C., Witters, L.A., and Kemp, B.E. (1997). Posttranslational modifications of the 5'-AMP-activated protein kinase beta1 subunit. J. Biol. Chem. *272*, 24475–24479. https://doi.org/10.1074/jbc.272.39.24475.
17. Oakhill, J.S., Chen, Z.P., Scott, J.W., Steel, R., Castelli, L.A., Ling, N., Macaulay, S.L., and Kemp, B.E. (2010). beta-Subunit myristoylation is the gatekeeper for initiating metabolic stress sensing by AMP-activated protein kinase (AMPK). Proc. Natl. Acad. Sci. USA *107*, 19237–19241. https://doi.org/10.1073/pnas.1009705107.
18. Warden, S.M., Richardson, C., O'Donnell, J., Jr., Stapleton, D., Kemp, B.E., and Witters, L.A. (2001). Post-translational modifications of the beta-1 subunit of AMP-activated protein kinase affect enzyme activity and cellular localization. Biochem. J. *354*, 275–283. https://doi.org/10.1042/0264-6021:3540275.
19. Giglione, C., and Meinnel, T. (2022). Mapping the myristoylome through a complete understanding of protein myristoylation biochemistry. Prog. Lipid Res. *85*, 101139. https://doi.org/10.1016/j.plipres.2021.101139.
20. Wright, M.H., Heal, W.P., Mann, D.J., and Tate, E.W. (2010). Protein myristoylation in health and disease. J. Chem. Biol. *3*, 19–35. https://doi.org/10.1007/s12154-009-0032-8.
21. Yuan, M., Song, Z.H., Ying, M.D., Zhu, H., He, Q.J., Yang, B., and Cao, J. (2020). N-myristoylation: from cell biology to translational medicine. Acta Pharmacol. Sin. *41*, 1005–1015. https://doi.org/10.1038/s41401-020-0388-4.
22. Morrison, K.R., Smiles, W.J., Ling, N.X.Y., Hoque, A., Shea, G., Ngoei, K.R.W., Yu, D., Murray-Segal, L., Scott, J.W., Galic, S., et al. (2022). An AMPKalpha2-specific phospho-switch controls lysosomal targeting for activation. Cell Rep. *38*, 110365. https://doi.org/10.1016/j.celrep.2022.110365.
23. Wen, Z., Jin, K., Shen, Y., Yang, Z., Li, Y., Wu, B., Tian, L., Shoor, S., Roche, N.E., Goronzy, J.J., and Weyand, C.M. (2019). N-myristoyltransferase deficiency impairs activation of kinase AMPK and promotes synovial tissue inflammation. Nat. Immunol. *20*, 313–325. https://doi.org/10.1038/s41590-018-0296-7.
24. Zhang, Y.L., Guo, H., Zhang, C.S., Lin, S.Y., Yin, Z., Peng, Y., Luo, H., Shi, Y., Lian, G., Zhang, C., et al. (2013). AMP as a low-energy charge signal autonomously initiates assembly of AXIN-AMPK-LKB1 complex for AMPK activation. Cell Metab. *18*, 546–555. https://doi.org/10.1016/j.cmet.2013.09.005.
25. Liang, J., Xu, Z.X., Ding, Z., Lu, Y., Yu, Q., Werle, K.D., Zhou, G., Park, Y.Y., Peng, G., Gambello, M.J., and Mills, G.B. (2015). Myristoylation confers noncanonical AMPK functions in autophagy selectivity and mitochondrial surveillance. Nat. Commun. *6*, 7926. https://doi.org/10.1038/ncomms8926.
26. Dite, T.A., Ling, N.X.Y., Scott, J.W., Hoque, A., Galic, S., Parker, B.L., Ngoei, K.R.W., Langendorf, C.G., O'Brien, M.T., Kundu, M., et al. (2017). The autophagy initiator ULK1 sensitizes AMPK to allosteric drugs. Nat. Commun. *8*, 571. https://doi.org/10.1038/s41467-017-00628-y.
27. Kim, S., Yang, X., Li, Q., Wu, M., Costyn, L., Beharry, Z., Bartlett, M.G., and Cai, H. (2017). Myristoylation of Src kinase mediates Src-induced and high-fat diet-accelerated prostate tumor progression in mice. J. Biol. Chem. *292*, 18422–18433. https://doi.org/10.1074/jbc.M117.798827.
28. Bultot, L., Jensen, T.E., Lai, Y.C., Madsen, A.L.B., Collodet, C., Kviklyte, S., Deak, M., Yavari, A., Foretz, M., Ghaffari, S., et al. (2016). Benzimidazole derivative small-molecule 991 enhances AMPK activity and glucose uptake induced by AICAR or contraction in skeletal muscle. Am. J. Physiol. Endocrinol. Metab. *311*, E706–E719. https://doi.org/10.1152/ajpendo.00237.2016.
29. Xiao, B., Sanders, M.J., Carmena, D., Bright, N.J., Haire, L.F., Underwood, E., Patel, B.R., Heath, R.B., Walker, P.A., Hallen, S., et al. (2013). Structural basis of AMPK regulation by small molecule activators. Nat. Commun. *4*, 3017. https://doi.org/10.1038/ncomms4017.

30. Alam, M.S. (2018). Proximity ligation assay (PLA). Curr. Protoc. Immunol. *123*, e58. https://doi.org/10.1002/cpim.58.

31. Cokorinos, E.C., Delmore, J., Reyes, A.R., Albuquerque, B., Kjøbsted, R., Jørgensen, N.O., Tran, J.L., Jatkar, A., Cialdea, K., Esquejo, R.M., et al. (2017). Activation of skeletal muscle AMPK promotes glucose disposal and glucose lowering in non-human primates and mice. Cell Metab. *25*, 1147–1159.e10. https://doi.org/10.1016/j.cmet.2017.04.010.

32. Dasgupta, B., Ju, J.S., Sasaki, Y., Liu, X., Jung, S.R., Higashida, K., Lindquist, D., and Milbrandt, J. (2012). The AMPK beta2 subunit is required for energy homeostasis during metabolic stress. Mol. Cell Biol. *32*, 2837–2848. https://doi.org/10.1128/MCB.05853-11.

33. Scott, J.W., Galic, S., Graham, K.L., Foitzik, R., Ling, N.X.Y., Dite, T.A., Issa, S.M.A., Langendorf, C.G., Weng, Q.P., Thomas, H.E., et al. (2015). Inhibition of AMP-activated protein kinase at the allosteric drug-binding site promotes islet insulin release. Chem. Biol. *22*, 705–711. https://doi.org/10.1016/j.chembiol.2015.05.011.

34. Treebak, J.T., Birk, J.B., Hansen, B.F., Olsen, G.S., and Wojtaszewski, J.F.P. (2009). A-769662 activates AMPK beta1-containing complexes but induces glucose uptake through a PI3-kinase-dependent pathway in mouse skeletal muscle. Am. J. Physiol. Cell Physiol. *297*, C1041–C1052. https://doi.org/10.1152/ajpcell.00051.2009.

35. Katwan, O.J., Alghamdi, F., Almabrouk, T.A., Mancini, S.J., Kennedy, S., Oakhill, J.S., Scott, J.W., and Salt, I.P. (2019). AMP-activated protein kinase complexes containing the beta2 regulatory subunit are up-regulated during and contribute to adipogenesis. Biochem. J. *476*, 1725–1740. https://doi.org/10.1042/BCJ20180714.

36. Scott, J.W., van Denderen, B.J.W., Jorgensen, S.B., Honeyman, J.E., Steinberg, G.R., Oakhill, J.S., Iseli, T.J., Koay, A., Gooley, P.R., Stapleton, D., and Kemp, B.E. (2008). Thienopyridone drugs are selective activators of AMP-activated protein kinase beta1-containing complexes. Chem. Biol. *15*, 1220–1230. https://doi.org/10.1016/j.chembiol.2008.10.005.

37. Garton, A.J., and Yeaman, S.J. (1990). Identification and role of the basal phosphorylation site on hormone-sensitive lipase. Eur. J. Biochem. *191*, 245–250. https://doi.org/10.1111/j.1432-1033.1990.tb19116.x.

38. Watt, M.J., Holmes, A.G., Pinnamaneni, S.K., Garnham, A.P., Steinberg, G.R., Kemp, B.E., and Febbraio, M.A. (2006). Regulation of HSL serine phosphorylation in skeletal muscle and adipose tissue. Am. J. Physiol. Endocrinol. Metab. *290*, E500–E508. https://doi.org/10.1152/ajpendo.00361.2005.

39. Pollard, A.E., Martins, L., Muckett, P.J., Khadayate, S., Bornot, A., Clausen, M., Admyre, T., Bjursell, M., Fiadeiro, R., Wilson, L., et al. (2019). AMPK activation protects against diet induced obesity through Ucp1-independent thermogenesis in subcutaneous white adipose tissue. Nat. Metab. *1*, 340–349. https://doi.org/10.1038/s42255-019-0036-9.

40. Mottillo, E.P., Desjardins, E.M., Crane, J.D., Smith, B.K., Green, A.E., Ducommun, S., Henriksen, T.I., Rebalka, I.A., Razi, A., Sakamoto, K., et al. (2016). Lack of adipocyte AMPK exacerbates insulin resistance and hepatic steatosis through Brown and Beige adipose tissue function. Cell Metab. *24*, 118–129. https://doi.org/10.1016/j.cmet.2016.06.006.

41. Garcia, D., Hellberg, K., Chaix, A., Wallace, M., Herzig, S., Badur, M.G., Lin, T., Shokhirev, M.N., Pinto, A.F.M., Ross, D.S., et al. (2019). Genetic liver-specific AMPK activation protects against diet-induced obesity and NAFLD. Cell Rep. *26*, 192–208.e6. https://doi.org/10.1016/j.celrep.2018.12.036.

42. Kozak, M. (1997). Recognition of AUG and alternative initiator codons is augmented by G in position +4 but is not generally affected by the nucleotides in positions +5 and +6. EMBO J. *16*, 2482–2492. https://doi.org/10.1093/emboj/16.9.2482.

43. Varshavsky, A. (2011). The N-end rule pathway and regulation by proteolysis. Protein Sci. *20*, 1298–1345. https://doi.org/10.1002/pro.666.

44. Timms, R.T., Zhang, Z., Rhee, D.Y., Harper, J.W., Koren, I., and Elledge, S.J. (2019). A glycine-specific N-degron pathway mediates the quality control of protein N-myristoylation. Science *365*, eaaw4912. https://doi.org/10.1126/science.aaw4912.

45. Qi, J., Gong, J., Zhao, T., Zhao, J., Lam, P., Ye, J., Li, J.Z., Wu, J., Zhou, H.M., and Li, P. (2008). Downregulation of AMP-activated protein kinase by Cidea-mediated ubiquitination and degradation in brown adipose tissue. EMBO J. *27*, 1537–1548. https://doi.org/10.1038/emboj.2008.92.

46. Yang, M., Zhang, D., Zhao, Z., Sit, J., Saint-Sume, M., Shabandri, O., Zhang, K., Yin, L., and Tong, X. (2020). Hepatic E4BP4 induction promotes lipid accumulation by suppressing AMPK signaling in response to chemical or diet-induced ER stress. FASEB J. *34*, 13533–13547. https://doi.org/10.1096/fj.201903292RR.

47. Hwang, C.S., Shemorry, A., and Varshavsky, A. (2010). N-terminal acetylation of cellular proteins creates specific degradation signals. Science *327*, 973–977. https://doi.org/10.1126/science.1183147.

48. Kats, I., Khmelinskii, A., Kschonsak, M., Huber, F., Knieß, R.A., Bartosik, A., and Knop, M. (2018). Mapping degradation signals and pathways in a eukaryotic N-terminome. Mol. Cell *70*, 488–501.e5. https://doi.org/10.1016/j.molcel.2018.03.033.

49. Shemorry, A., Hwang, C.S., and Varshavsky, A. (2013). Control of protein quality and stoichiometries by N-terminal acetylation and the N-end rule pathway. Mol. Cell *50*, 540–551. https://doi.org/10.1016/j.molcel.2013.03.018.

50. Ali, N., Ling, N., Krishnamurthy, S., Oakhill, J.S., Scott, J.W., Stapleton, D.I., Kemp, B.E., Anand, G.S., and Gooley, P.R. (2016). beta-subunit myristoylation functions as an energy sensor by modulating the dynamics of AMP-activated Protein Kinase. Sci. Rep. *6*, 39417. https://doi.org/10.1038/srep39417.

51. Chen, L., Jiao, Z.H., Zheng, L.S., Zhang, Y.Y., Xie, S.T., Wang, Z.X., and Wu, J.W. (2009). Structural insight into the autoinhibition mechanism of AMP-activated protein kinase. Nature *459*, 1146–1149. https://doi.org/10.1038/nature08075.

52. Moore, I., and Murphy, A. (2009). Validating the location of fluorescent protein fusions in the endomembrane system. Plant Cell *21*, 1632–1636. https://doi.org/10.1105/tpc.109.068668.

53. Carling, D., Clarke, P.R., Zammit, V.A., and Hardie, D.G. (1989). Purification and characterization of the AMP-activated protein kinase. Copurification of acetyl-CoA carboxylase kinase and 3-hydroxy-3-methylglutaryl-CoA reductase kinase activities. Eur. J. Biochem. *186*, 129–136. https://doi.org/10.1111/j.1432-1033.1989.tb15186.x.

54. Voss, M., Paterson, J., Kelsall, I.R., Martín-Granados, C., Hastie, C.J., Peggie, M.W., and Cohen, P.T.W. (2011). Ppm1E is an in cellulo AMP-activated protein kinase phosphatase. Cell. Signal. *23*, 114–124. https://doi.org/10.1016/j.cellsig.2010.08.010.

55. Woods, A., Williams, J.R., Muckett, P.J., Mayer, F.V., Liljevald, M., Bohlooly-Y, M., and Carling, D. (2017). Liver-specific activation of AMPK prevents steatosis on a high-fructose diet. Cell Rep. *18*, 3043–3051. https://doi.org/10.1016/j.celrep.2017.03.011.

56. Rhein, P., Desjardins, E.M., Rong, P., Ahwazi, D., Bonhoure, N., Stolte, J., Santos, M.D., Ovens, A.J., Ehrlich, A.M., Sanchez Garcia, J.L., et al. (2021). Compound- and fiber type-selective requirement of AMPKgamma3 for insulin-independent glucose uptake in skeletal muscle. Mol. Metab. *51*, 101228. https://doi.org/10.1016/j.molmet.2021.101228.

57. Zhang, Z., Zhang, H., Li, B., Meng, X., Wang, J., Zhang, Y., Yao, S., Ma, Q., Jin, L., Yang, J., et al. (2014). Berberine activates thermogenesis in white and brown adipose tissue. Nat. Commun. *5*, 5493. https://doi.org/10.1038/ncomms6493.

58. Yang, J., Maika, S., Craddock, L., King, J.A., and Liu, Z.M. (2008). Chronic activation of AMP-activated protein kinase-alpha1 in liver leads to decreased adiposity in mice. Biochem. Biophys. Res. Commun. *370*, 248–253. https://doi.org/10.1016/j.bbrc.2008.03.094.

59. Yang, H., Wang, H., and Jaenisch, R. (2014). Generating genetically modified mice using CRISPR/Cas-mediated genome engineering. Nat. Protoc. *9*, 1956–1968. https://doi.org/10.1038/nprot.2014.134.

60. Ducommun, S., Ford, R.J., Bultot, L., Deak, M., Bertrand, L., Kemp, B.E., Steinberg, G.R., and Sakamoto, K. (2014). Enhanced activation of cellular

AMPK by dual-small molecule treatment: AICAR and A769662. Am. J. Physiol. Endocrinol. Metab. *306*, E688–E696. https://doi.org/10.1152/ajpendo.00672.2013.

61. Scott, J.W., Ling, N., Issa, S.M.A., Dite, T.A., O'Brien, M.T., Chen, Z.P., Galic, S., Langendorf, C.G., Steinberg, G.R., Kemp, B.E., and Oakhill, J.S. (2014). Small molecule drug A-769662 and AMP synergistically activate naive AMPK independent of upstream kinase signaling. Chem. Biol. *21*, 619–627. https://doi.org/10.1016/j.chembiol.2014.03.006.

62. Iseli, T.J., Oakhill, J.S., Bailey, M.F., Wee, S., Walter, M., van Denderen, B.J., Castelli, L.A., Katsis, F., Witters, L.A., Stapleton, D., et al. (2008). AMP-activated protein kinase subunit interactions: beta1:gamma1 association requires beta1 Thr-263 and Tyr-267. J. Biol. Chem. *283*, 4799–4807. https://doi.org/10.1074/jbc.M708298200.

63. Schindelin, J., Arganda-Carreras, I., Frise, E., Kaynig, V., Longair, M., Pietzsch, T., Preibisch, S., Rueden, C., Saalfeld, S., Schmid, B., et al. (2012). Fiji: an open-source platform for biological-image analysis. Nat. Methods *9*, 676–682. https://doi.org/10.1038/nmeth.2019.

64. Bolte, S., and Cordelières, F.P. (2006). A guided tour into subcellular colocalization analysis in light microscopy. J. Microsc. *224*, 213–232. https://doi.org/10.1111/j.1365-2818.2006.01706.x.

65. Manders, E.M.M., Verbeek, F.J., and Aten, J.A. (1993). Measurement of co-localization of objects in dual-colour confocal images. J. Microsc. *169*, 375–382. https://doi.org/10.1111/j.1365-2818.1993.tb03313.x.

66. Franklin, K.B.J., and Paxinos, G. (2008). The Mouse Brain in Stereotaxic Coordinates, 3rd Edition (Elsevier).

67. Hamilton, S.R., Stapleton, D., O'Donnell, J.B., Jr., Kung, J.T., Dalal, S.R., Kemp, B.E., and Witters, L.A. (2001). An activating mutation in the gamma1 subunit of the AMP-activated protein kinase. FEBS Lett. *500*, 163–168. https://doi.org/10.1016/s0014-5793(01)02602-3.

68. Dzamko, N., van Denderen, B.J.W., Hevener, A.L., Jørgensen, S.B., Honeyman, J., Galic, S., Chen, Z.P., Watt, M.J., Campbell, D.J., Steinberg, G.R., and Kemp, B.E. (2010). AMPK beta1 deletion reduces appetite, preventing obesity and hepatic insulin resistance. J. Biol. Chem. *285*, 115–122. https://doi.org/10.1074/jbc.M109.056762.

69. Fullerton, M.D., Galic, S., Marcinko, K., Sikkema, S., Pulinilkunnil, T., Chen, Z.P., O'Neill, H.M., Ford, R.J., Palanivel, R., O'Brien, M., et al. (2013). Single phosphorylation sites in Acc1 and Acc2 regulate lipid homeostasis and the insulin-sensitizing effects of metformin. Nat. Med. *19*, 1649–1654. https://doi.org/10.1038/nm.3372.

70. Mina, A.I., LeClair, R.A., LeClair, K.B., Cohen, D.E., Lantier, L., and Banks, A.S. (2018). CalR: a web-based analysis tool for indirect calorimetry experiments. Cell Metab. *28*, 656–666.e1. https://doi.org/10.1016/j.cmet.2018.06.019.

STAR★METHODS

KEY RESOURCES TABLE

REAGENT or RESOURCE	SOURCE	IDENTIFIER
Antibodies		
ACC (rabbit monoclonal)	Cell Signaling Technology	Cat# 3676; clone C83B10; RRID: AB_2219397
β-actin (mouse monoclonal)	Sigma-Aldrich	Cat# A2228; clone AC-74; RRID: AB_476697
pan-actin (rabbit polyclonal)	Cell Signaling Technology	Cat# 4968; RRID: AB_2313904
ACC1 (rabbit polyclonal)	Cell Signaling Technology	Cat# 4190; RRID: AB_10547752
pan AMPK α (rabbit polyclonal)	Cell Signaling Technology	Cat# 2532; RRID: AB_330331
pan AMPK α (2-20) (rabbit polyclonal)	Hamilton et al., 2001	N/A
AMPK α1 (rabbit polyclonal)	Millipore	Cat# 07-350; RRID: AB_310542
AMPK α1 (344-358) (rabbit polyclonal)	Bultot et al., 2016	N/A
AMPK α2 (rabbit polyclonal)	Cell Signaling Technology	Cat# 2757; RRID: AB_560858
pan AMPK β (rabbit monoclonal)	Cell Signaling Technology	Cat# 4150; clone 57C12; RRID: AB_10828832
AMPK β1 (rabbit polyclonal)	Cell Signaling Technology	Cat# 12063; RRID: AB_2797812
AMPK β1 (mouse monoclonal)	Signalway Antibody	Cat# 27201
AMPK β2 (rabbit polyclonal)	Cell Signaling Technology	Cat# 4148; RRID: AB_560862
AMPK γ1 (rabbit monoclonal)	Abcam	Cat# ab32508; RRID: AB_722769
AMPK γ1 (rabbit monoclonal)	Abcam	Cat# 1569-1, RRID: AB_562359
c-fos (rabbit polyclonal)	Abcam	Cat# ab190289, RRID: AB_2134500
HSL (rabbit polyclonal)	Watt et al., 2006	N/A
LAMP1 (rat monoclonal)	DSHB	Cat# 1D4B, RRID: AB_2134500
OXPHOS Rodent Antibody Cocktail (mouse monoclonal)	Abcam	Cat# ab110413; RRID: AB_2629281
PPM1A (mouse monoclonal)	Abcam	Cat# ab14824; clone p6c7; RRID: AB_301501
PPM1A (rabbit polyclonal)	Proteintech	Cat# 12961-1-AP; RRID: AB_2169763
PPM1B (rabbit polyclonal)	Proteintech	Cat# 13193-1-AP; RRID: AB_10644118
Raptor (rabbit monoclonal)	Cell Signaling Technology	Cat# 2280; clone 24C12; RRID: AB_561245
α/β-tubulin (rabbit polyclonal)	Cell Signaling Technology	Cat# 2148; RRID: AB_2288042
UCP1 (rabbit polyclonal)	Alpha Diagnostic	Cat# UCP11-A; RRID: AB_1624298
UCP1 (rabbit polyclonal)	Abcam	Cat# ab10983; RRID: AB_2241462
ULK1 (rabbit polyclonal)	Proteintech	Cat# 20986-1-AP; RRID: AB_2878783
ACC pS79/S212 (polyclonal rabbit)	Cell Signaling Technology	Cat# 3361; RRID: AB_330337
AMPK α pT172 (rabbit monoclonal)	Cell Signaling Technology	Cat# 2535: RRID: AB_331250
HSL pS565 (rabbit polyclonal)	Watt et al., 2006	N/A
Raptor pS792 (rabbit polyclonal)	Cell Signaling Technology	Cat# 2083; RRID: AB_2249475
ULK1 pS555 (rabbit monoclonal)	Cell Signaling Technology	Cat# 5869; clone D1H4: RRID: AB_10707365
Alexa Fuor 680 goat anti-rabbit IgG	Thermo Fisher Scientific	Cat# A-21109; RRID: AB_2535758
Alexa Fluor 680 goat anti-mouse IgG	Thermo Fisher Scientific	Cat# A-21057; RRID: AB_2535723
Alexa Fluor 790 goat anti-rabbit IgG	Thermo Fisher Scientific	Cat# A-11369; RRID: AB_2534142
Alexa Fluor 488 goat anti-mouse IgG	Thermo Fisher Scientific	Cat# A-11001; RRID: AB_2534069
Alexa Fluor 647 goat anti-rat IgG	Thermo Fisher Scientific	Cat# A-21247; RRID: AB_141778
Biotinylated goat anti-rabbit IgG	Agilent	Cat# E0432: RRID: AB_2313609

(*Continued on next page*)

Continued

REAGENT or RESOURCE	SOURCE	IDENTIFIER
DyLight goat-anti-rabbit IgG	Abcam	Cat# 96899; RRID: AB_10679361
HRP goat anti-rabbit IgG	Agilent Dako	Cat# P0448; RRID: AB_2617138
HRP goat anti-mouse IgG	Agilent Dako	Cat# P0447; RRID: AB_2617137
Bacterial and virus strains		
Escherichia coli Rosetta 2 (DE3)	Merck	Cat# 71397
Chemicals, peptides, and recombinant proteins		
5-Aminoimidazole-4-carboxamide-1-b-D-ribofuranoside (AICAR)	Toronto Research Chemicals	Cat# A611700; Cas: 2626-69-2
Collagen coating solution	Sigma-Aldrich	Cat# 125-50
cOmplete protease inhibitor cocktail	Sigma-Aldrich	Cat# 11697498001
DMEM, high glucose	Thermo Fisher Scientific	Cat# 11965084
D.P.X. mounting medium	Sigma-Aldrich	Cat# 317616
Faramount mounting medium	Agilent Dako	Cat# S6025
Fluoromount G mounting medium	Sigma-Aldrich	Cat# F4680
Fluoroshield with DAPI mounting medium	Sigma-Aldrich	Cat# F6057
Formaldehyde, 37% in H_2O	Sigma-Aldrich	Cat# 252549; Cas: 50-00-0
FuGENE HD	Promega	Cat# E2311
D-Glucose	Sigma-Aldrich	Cat# G8270; Cas: 50-99-7
Glyceryl tripalmitate (TLC standard)	Sigma-Aldrich	Cat# T5888; Cas: 555-44-2
Hoechst 33258 solution	Sigma-Aldrich	Cat# 94403; Cas: 23,491-45-4
Insulin (Actrapid)	Novo Nordisk	Cat #:169,625
Intralipid	Sigma-Aldrich	Cat# I141; Cas: 68,890-65-3
Liberase TM Research Grade	Roche Diagnostics	Cat# 26628-22-8
Lipofectamine RNAiMAX	Invitrogen	Cat# 13778075
Medium 199	Thermo Fisher Scientific	Cat# 11150059
Oil Red O	Sigma-Aldrich	Cat# O0625; Cas: 1320-06-5
Restore Plus Western Blotting Stripping Buffer	Thermo Fisher Scientific	Cat# 46430
SYPRO™ Orange Protein Gel Stain	Thermo Fisher Scientific	Cat# S6651
Streptavidin, Alexa Fluor 488 conjugate	Thermo Fisher Scientific	Cat# S11223
Streptavidin, Alexa Fluor 680 conjugate	Thermo Fisher Scientific	Cat# S21378
Streptavidin, Alexa Fluor 790 conjugate	Thermo Fisher Scientific	Cat# S11378
Streptavidin, HRP conjugate	Abcam	Cat# ab7403
Tissue-Tek O.C.T compound	ProSciTech	Cat# 4583
SAMS synthetic peptide substrate HMRSAMSGLHLVKRR-NH2	Purar Chemicals	N/A
TRIzol Reagent	Thermo Fisher Scientific	Cat#15596026
[^{3}H] acetate (sodium)	PerkinElmer	Cat# NET003H005MC
[1-^{14}C] palmitic acid	PerkinElmer	Cat# NEC075H250UC
[γ-^{32}P] ATP	PerkinElmer	Cat# BLU002Z500UC
Critical commercial assays		
AmpliTaq Gold™ DNA Polymerase kit	Thermo Fisher Scientific	Cat# 4311806
Avidin/Biotin Blocking Kit	Vector Laboratories	Cat# SP-2001
Click-IT™ Myristic Acid, Azide (12-Azidododecanoic Acid) kit	Thermo Fisher Scientific	Cat# C10268
Click-iT™ Protein Reaction Buffer Kit	Thermo Fisher Scientific	Cat# C10276
DAB Substrate Kit	Vector Laboratories	Cat# SK-4100

(*Continued on next page*)

Continued

REAGENT or RESOURCE	SOURCE	IDENTIFIER
Duolink In Situ Red Starter Kit Mouse/Rabbit	Sigma-Aldrich	Cat# DUO92101
Glycogen Assay Kit	Abcam	Cat# ab65620
LabAssay Triglyceride	Wako	Cat# LABTRIG-M1
Mouse insulin ELISA	Mercodia	Cat# 10-1247-01
SuperScript™ IV First-Strand Synthesis System	Thermo Fisher Scientific	Cat# 18091050
Triglyceride Assay Kit	Abcam	Cat# ab65336
VECTASTAIN ABC Peroxidase Kit	Vector Laboratories	Cat# PK-4005
18S TaqMan® Gene Expression Assay	Thermo Fisher Scientific	Cat# Hs99999901_s1
Acaca TaqMan® Gene Expression Assay	Thermo Fisher Scientific	Cat# Mm01304277_m1
Acacb TaqMan® Gene Expression Assay	Thermo Fisher Scientific	Cat# Mm01204683_m1
Acadl TaqMan® Gene Expression Assay	Thermo Fisher Scientific	Cat# Mm00599660_m1
Acadm TaqMan® Gene Expression Assay	Thermo Fisher Scientific	Cat# Mm00431611_m1
Actb TaqMan® Gene Expression Assay	Thermo Fisher Scientific	Cat# Mm02619580_g1
Atp2a1 TaqMan® Gene Expression Assay	Thermo Fisher Scientific	Cat# Mm01275320_m1
Ckmt2 TaqMan® Gene Expression Assay	Thermo Fisher Scientific	Cat# Mm01285553_m1
Cpt1b TaqMan® Gene Expression Assay	Thermo Fisher Scientific	Cat# Mm00487200_m1
Cs TaqMan® Gene Expression Assay	Thermo Fisher Scientific	Cat# Mm00466043_m1
Elovl3 TaqMan® Gene Expression Assay	Thermo Fisher Scientific	Cat# Mm00468164_m1
Fasn TaqMan® Gene Expression Assay	Thermo Fisher Scientific	Cat# Mm00662319_m1
Hadh TaqMan® Gene Expression Assay	Thermo Fisher Scientific	Cat# Mm00492535_m1
Myh4 TaqMan® Gene Expression Assay	Thermo Fisher Scientific	Cat# Mm01332541_m1
Prkaa1 TaqMan® Gene Expression Assay	Thermo Fisher Scientific	Cat# Mm01296700_m1
Prkaa1 TaqMan® Gene Expression Assay	Thermo Fisher Scientific	Cat# Mm01264789_m1
Prkab1 TaqMan® Gene Expression Assay	Thermo Fisher Scientific	Cat# Mm01257133_m1
Prkab2 TaqMan® Gene Expression Assay	Thermo Fisher Scientific	Cat# Mm01201921_m1
Ppara TaqMan® Gene Expression Assay	Thermo Fisher Scientific	Cat# Mm00440939_m1
Ppargc1a TaqMan® Gene Expression Assay	Thermo Fisher Scientific	Cat# Mm00447183_m1
Ryr1 TaqMan® Gene Expression Assay	Thermo Fisher Scientific	Cat# Mm01175811_m1
Scd1 TaqMan® Gene Expression Assay	Thermo Fisher Scientific	Cat# Mm00772290_m1
Sdhd TaqMan® Gene Expression Assay	Thermo Fisher Scientific	Cat# Mm00546511_m1
Srebf1 TaqMan® Gene Expression Assay	Thermo Fisher Scientific	Cat# Mm00550338_m1
Ucp1 TaqMan® Gene Expression Assay	Thermo Fisher Scientific	Cat# Mm01244861_m1
Experimental models: Cell lines		
AMPK $\beta1^{G2A}$ immortalized mouse embryonic fibroblasts (β1-G2A KI)	This study	N/A
AMPK $\beta2^{G2A}$ immortalized mouse embryonic fibroblasts (β2-G2A KI)	This study	N/A
AMPK $\beta1^{G2A}/\beta2^{G2A}$ immortalized mouse embryonic fibroblasts (β1/β2-G2A DKI)	This study	N/A
Wild type immortalized mouse embryonic fibroblasts	This study	N/A
Sf21 insect cells	Thermo Fisher Scientific	Cat# 11497013
Experimental models: Organisms/strains		
Mouse: C57BL/6J-Prkab1^{em1Ausb}	This study	N/A
Mouse: C57BL/6J-Prkab2^{em1Ausb}	This study	N/A

(*Continued on next page*)

Continued

REAGENT or RESOURCE	SOURCE	IDENTIFIER
Oligonucleotides		
Human AMPK β1 G2A For: GGTACCATGGCCAATACCAGCAGTGAGCGC	Sigma-Aldrich	N/A
Human AMPK β1 G2A Rev: GCGCTCACTGCTGGTATTGGCCATGGTACC	Sigma-Aldrich	N/A
Recombinant DNA		
pBSSVD2005 SV40 large T-antigen expression	Gift, D. Ron	Addgene RRID: 21,826
pFASTBAC1-FLAG-N-TEV-CaMKKβ	Iseli et al., 2008	N/A
pETDuet-1 human AMPK α1(N-term 6xhis fusion)/γ1	Scott et al., 2014	N/A
pRSFDuet-1 human AMPK β1	Scott et al., 2014	N/A
pRSFDuet-1 human AMPK β1 G2A	This study	N/A
Software and algorithms		
Fiji/ImageJ	NIH; Schindelin et al., 2012	https://imagej.net; RRID: SCR_003070
JACoP	Bolte and Cordelieres, 2006	https://imagej.net/plugins/jacop
Image Studio Lite 5	LI-COR Biosciences	https://www.licor.com/bio/products/software/image_studio_lite; RRID: SCR_013715
GraphPad Prism 9	GraphPad Software	https://www.graphpad.com; RRID: SCR_002798
Other		
Anti-FLAG M2 affinity gel	Sigma-Aldrich	Cat# D2220
Bolt 4-12% Bis-Tris mini protean gels	Thermo Fisher Scientific	Cat# NW04125BOX
Cation-exchange paper	Produced in-house	https://www.svi.edu.au/resources/phosphocellulose_paper/
Glass coverslips No 1.5	Epredia	Cat# MENZCB00120RAC20
Immobilon-P PVDF membrane	Millipore	Cat# IPVH00010
Mouse chow diet	Ridley AgriProducts	Cat# RID15635
Mouse high-fat diet (23% fat)	Specialty Feeds	Cat# SF04-027
μ-slide angiogenesis chamber	Ibidi	Cat# 81506
Nitrocellulose membrane	LI-COR Biosciences	Cat# 926-31092
Protein A Agarose Fast Flow	Sigma-Aldrich	Cat# P3476
Protein G Sepharose 4 Fast Flow	GE Healthcare	Cat# 17-0618-01
Super RXN Medical X-ray Film	Fujifilm	Cat# 47410-19289
TLC UNISIL Silica GF plates	Analtech	Cat# 40011

RESOURCE AVAILABILITY

Lead contact

Further information and requests for resources and reagents should be directed to and will be fulfilled by the lead contact, Sandra Galic (sgalic@svi.edu.au).

Materials availability

Mouse lines, cell lines and plasmids generated in this study are available upon request.

Data and code availability

- All data reported in this paper will be shared by the lead contact upon request.
- This paper does not report original code.
- All additional information required to reanalyze the data reported in this paper is available from the lead contact upon request.

EXPERIMENTAL MODEL AND SUBJECT DETAILS

Mice and ethics statement

Prkab1^{G2A} (β1-G2A) and *Prkab2*^{G2A} (β2-G2A) KI mice were produced by the Mouse Engineering Garvan/ABR (MEGA) Facility using CRISPR/Cas9 gene targeting in C57BL/6J mouse embryos following established molecular and animal husbandry techniques.[59] Single guide RNAs (sgRNA) were based on target sites in exon 2 of *Prkab1* (GAGCAGCGAGCGCGCCGCGC*TGG*) and *Prkab2* (TAC CAGCGAGCGGGTGTCC*GGG*) (protospacer-associated motif = PAM italicized and underlined). In each case the specific sgRNA (15 ng/μL) was microinjected into the nucleus and cytoplasm of C57BL/6J zygotes together with polyadenylated *S. pyogenes* Cas9 mRNA (30 ng/μL) and a gene-specific 150 base single-stranded, anti-sense, deoxy-oligonucleotide homologous recombination substrate (15 ng/μL). For *Prkab1* the oligonucleotide encoded the G2A (GGC>GCC) substitution plus a PAM-inactivating silent mutation in the L11 codon (CTG>CTC), whilst for *Prkab2* the oligonucleotide encoded the G2A (GGA>GCA) substitution plus a PAM-inactivating silent mutation in the G11 codon (GGG>GGC) (Figure S1). Founder males heterozygous for alleles that had been successfully modified by homologous recombination were backcrossed with C57BL/6J females to establish the β1-G2A and β2 G2A lines.

Breeding of β1-G2A and β2 G2A mouse lines was performed using heterozygous carriers of the KI mutation with biannual backcrosses to the C57BL/6JArc strain. For genotyping, tail samples were analyzed by TransnetYX using TaqMan-based real-time PCR. Mice homozygous for either the β1-G2A or β2-G2A mutation were crossed to generate β1/β2-G2A DKI mice for the isolation of mouse embryonic fibroblasts. Homozygous β1-G2A KI mice and WT mice derived from the same heterozygous founders were used for all other experiments. The study included only male mice due to limited availability of females for age-matched cohorts for metabolic studies while ensuring that sufficient females were available for colony maintenance. Mice were housed in pathogen-free microisolator cages on a 12-h light-dark cycle. Mice were fed a standard chow diet (9% fat, 20% protein and 29% starch, with 12.8 MJ/kg of digestible energy, Ridley Agriproducts) or placed at 6-7-weeks of age on an HFD (23.5% fat, 18.4% protein and 22.8% starch, with 17 MJ/kg digestible energy, Specialty Feeds) for 12-13 weeks with *ad libitum* access to water. For all experiments, mice were age-matched within two-four-weeks of age, but otherwise randomized to their respective groups. The St. Vincent's Hospital (Melbourne, Australia) Animal Ethics Committee approved all experimental procedures (AEC 025/15 and AEC 013/19) in accordance with the National Health and Medical Research Council of Australia's (NHMRC) guidelines for the Ethical and Humane Use of Animals in research and Australian code of practice for the care and use of animals for scientific purposes (eighth Edition 2013).

Immortalized mouse embryonic fibroblasts

Mouse embryonic fibroblasts (MEFs) were isolated from homozygous WT, β1-G2A KI, β2-G2A KI or β1/β2-G2A DKI embryos at days 12–13 post coitum. The head and internal organs were removed, and the remaining embryo body minced and trypsinized. After adding DMEM supplemented with 10% FBS and 1% penicillin-streptomycin, cells were centrifuged (500 g, 5 min, 4°C) and medium replaced and the cell suspension was passed through a 40-μm cell strainer and plated in 10-cm dishes. Cells were cultured in DMEM supplemented with 10% FBS and 1% penicillin-streptomycin and passaged at 1:2 or 1:4 when confluent. MEFs were immortalized by transfection with an SV40 large T-antigen expression construct using Fugene HD transfection reagent (Promega).

METHOD DETAILS

Metabolic studies

Body composition analysis was performed by nuclear magnetic resonance imaging (Whole Body Composition Analyzer (EchoMRI)). Analysis of metabolic parameters, including energy expenditure, ambulatory activity, food intake and substrate preference was performed in 13-14-week-old mice using the Comprehensive Laboratory Animal Monitoring System (CLAMS, Columbus Instruments). Mice were individually housed with free access to water and either a standard laboratory chow or HFD and kept on a 12-h light/dark cycle and temperature controlled at 21°C throughout the experiment. Volumes of oxygen consumption (VO_2) and carbon dioxide production (VCO_2), food intake and ambulatory activity were measured continuously in 18-min intervals for 48 h after a 24-h acclimatization period. Food intake was recorded via scale measurement of a center-feeder while ambulatory activity was determined by the breaking of infrared beams within the cages. Respiratory exchange ratio (RER = VCO_2/VO_2) and energy expenditure (Heat = (3.815 + 1.232*RER)*VO_2) were calculated from the measured gas exchange data. Energy expenditure data were normalized to lean mass measured at day 1 of the experiment.

Blood glucose concentrations were measured in 22-23-week-old chow-fed and 20-21-week-old HFD-fed mice on tail blood using a hand-held glucometer (Accu-Check Performa, Roche Diagnostics). For measurement of serum insulin and serum triglyceride concentrations, whole blood samples were collected using the submandibular method from 20 to 21-week-old chow and 19-20-week-old HFD-fed mice and left to clot at room temperature for 30 min followed by centrifugation at 1,500 g for 10 min. Insulin concentration was determined from supernatants using a mouse insulin ELISA (Mercodia). Triglyceride levels were analyzed using a colorimetric assay (LabAssay Triglyceride Kit, Wako).

Tissues for biochemical and histological analyses were dissected from 20 to 24-week-old chow or 19-22-week-old HFD-fed mice anesthetized by ketamine/xylazine injection and snap-frozen in liquid nitrogen until further analyses or fixed in 10% formalin.

For glycogen measurements, tissue was homogenized in ddH_2O on ice using a hand-held homogenizer. After heating at 100°C for 10 min, samples were centrifuged at 18,000 g for 10 min and glycogen concentrations determined from the supernatant using the Glycogen Assay Kit (Abcam). For triglyceride assays, liver tissue was homogenized in 6.5% NP-40/ddH2O at room temperature. Triglycerides were solubilized using 5 cycles of heating at 90°C for 3 min and cooling to room temperature. Samples were centrifuged at 21,000 g, 4°C and supernatants assayed using the Triglyceride Assay Kit (Abcam). Separate liver biopsies from the same animals were assayed for total fat content using the biopsy function of the EchoMRI Body Composition Analyzer.

Insulin, glucose and lipid tolerance testing

Tolerance tests were performed in 13-14-week-old chow- and 12-13-week-old HFD-fed mice. For insulin tolerance testing, mice were fasted for 4 h followed by intraperitoneal insulin (Actrapid, Novo Nordisk) injection with 0.6 IU/kg lean mass for chow-fed animals and 1.2 IU/kg for HFD-fed animals. For glucose tolerance tests, mice were fasted for 6 h and injected with 2 g D-glucose/kg lean mass for the chow-fed condition and 1 g D-glucose/kg lean mass for HFD-fed mice. D-glucose (Sigma-Aldrich) was dissolved in saline. Blood glucose concentrations were measured from tail blood using a hand-held glucometer (AccuCheck Performa, Roche Diagnostics). For lipid tolerance testing, chow-fed β1-G2A KI and WT mice were fasted for 16 h followed by gavage with 10 mL/kg Intralipid (20% soybean oil v/v, Sigma-Aldrich). Blood samples were obtained from the tail tip immediately before gavage (T = 0) and at every 45-60 min after the lipid challenge. Blood was allowed to clot, and serum triglycerides concentrations analyzed using the LabAssay Triglyceride Kit (Wako). Area under the curve calculations were performed using GraphPad Prism Software.

Histological analyses

For hematoxylin/eosin (H/E) staining, tissue samples from chow-fed (20-24 weeks) or HFD-fed (age 19-22 weeks) mice were fixed at room temperature for 48 h in 10% neutral buffered formalin and transferred to 70% ethanol. After processing, samples were embedded in paraffin and sectioned at 5 μm using a microtome. Sections were de-waxed in histolene and after rehydration stained in Mayer's hematoxylin for 5 min, followed by blueing in Scott's tap water and incubation with eosin for 3 min. Samples were dehydrated and mounted using dibutylphthalate polystyrene xylene. Subcutaneous adipocyte size was determined by measuring the area of cells in 3–4 representative images per section and 6 mice per genotype using ImageJ. The frequency distribution of the number of cells per area size (bin 100 μm^2) was calculated using GraphPad Prism 9 software. For Oil Red O (ORO) staining, tissues were frozen in O.C.T. compound (ProSciTech) and sectioned on a cryostat at 8 μm. Sections were fixed in 10% buffered formalin, washed in water and 60% isopropanol before staining in 60% ORO working solution for 15 min (stock solution: 1% ORO powder in isopropanol). The slides were then washed in 60% isopropanol and distilled water. To counterstain, sections were stained in Mayer's hematoxylin for 1 min and mounted with Faramount mounting medium (Agilent-Dako). The area of ORO staining was determined from averages of 3 representative images per mouse with 6 mice per diet and genotype using the thresholding function in ImageJ. Images were taken using a Leica DM-RB light microscope and relayed with an Olympus DP72 camera.

For UCP1 immunohistochemistry, subcutaneous adipose tissue was fixed with 10% formalin, embedded in paraffin and sectioned on a microtome at a thickness of 5 μm. Sections were de-waxed in histolene and after rehydration boiled in citrate antigen retrieval buffer (10 mM sodium citrate, pH 6.5) for 15 min. Endogenous peroxidases were quenched by incubation with 3% H_2O_2 in PBS for 15 min. Sections were blocked by incubation with 5% normal goat serum (NGS) in PBS for 40 min, followed by 15 min incubations each with avidin D and biotin (Avidin/Biotin Blocking Kit, Vector Laboratories). Primary rabbit anti-UCP1 antibody (Abcam) was added at a concentration of 1: 500 in PBS/5% NGS for 2 h at room temperature. After subsequent washes with PBS, sections were incubated with secondary biotinylated goat anti-rabbit antibody (Agilent Technologies) at 1:250 in PBS/5% NGS for 1 h at room temperature. Following washes in PBS, secondary antibody binding was detected by incubating sections with VECTASTAIN ABC Peroxidase kit (Vector Laboratories) and DAB substrate kit (Vector Laboratories) as per manufacturer's instructions. Sections were counterstained, dehydrated and mounted using D.P.X (Sigma-Aldrich). Images were taken under bright-field conditions using an Olympus BX61 microscope and Olympus DP71 camera.

Western blotting

Cells and tissues were homogenized in lysis buffer containing protease and phosphatase inhibitors as previously described.[36,60] For immunoblotting of MEF lysates, 20 μg protein was resolved using Bolt 4-12%, Bis-Tris mini protein gels (Thermo Fisher Scientific). Protein gels were transferred onto nitrocellulose membranes (LI-COR Biosciences) and incubated in primary antibody diluted in Tris-buffered saline/0.1% Tween 20 containing 5% BSA overnight at 4°C. After 1-h incubation with secondary antibody conjugated to AF-680 at room temperature, membranes were scanned using Odyssey CLx Infrared Scanner. For immunoblotting of tissue homogenates, 20-50 μg total lysate was separated via SDS-PAGE, followed by transfer to an Immobilon-P PVDF membrane (Merck Millipore). Membranes were incubated overnight at 4°C with primary antibody in PBS-Tween 20, followed by incubation with HRP-conjugated secondary antibodies in PBS-Tween 20 supplemented with 2.5% skim milk. Proteins were detected by enhanced chemiluminescence and exposure to Super RX Medical X-ray Film (Fujifilm). Total ACC was determined by overnight incubation with streptavidin-HRP. To control for protein loading, signal obtained for phosphorylated ACC and AMPK were normalized to total ACC or AMPK α signal obtained from the same membrane after incubation in Restore PLUS Western blot stripping buffer (Thermo Fisher Scientific). The volume densities of the protein signals were quantified using Image Studio software (LI-COR Biosciences).

Protein expression and purification of *E. Coli*-expressed AMPK and CaMKK2

AMPK β1-G2A mutation was introduced into a pRSFDuet-1 human AMPK β1 expression construct[61] by mutagenesis PCR using Pfu Turbo DNA polymerase (Agilent) (forward primer: 5′-ggtaccatggccaataccagcagtgagcgc; reverse primer: 5′- gcgctcactgctggtattggc-catggtacc). The resulting pRSFDuet-1 AMPK β1(G2A) construct was sequence verified. Recombinant full-length AMPK α1β1γ1 and α1β1(G2A)γ1 were expressed in E. coli Rosetta 2 (DE3) (Merck Millipore) as hexahistidine-tagged complexes after double-transformation of pETDuet-1 (MCS1: his-α1; MCS2: γ1) and pRSFDuet-1 (MCS1: β1 WT or G2A; MCS2: empty).[61] Expression cultures were grown at 37°C in Luria-Bertani broth supplemented with 100 μg/mL ampicillin and 50 μg/mL kanamycin. Cultures shaking at 120 rpm in PYREX 2800 mL Fernbach-style culture flasks with baffles (Corning) were grown to an optical density (OD600) of 3.0 before induction with 500 μM isopropyl-β-D-1-thiogalactopyranoside (IPTG; Gold Biotechnology) and incubation overnight at 16°C. Cell pellets were resuspended in lysis buffer (50 mM TRIS pH 7.6, 500 mM NaCl, 5% (v/v) glycerol, 50 mM imidazole, 2 mM β-mercaptoethanol, 0.01 mM leupeptin, 0.1 mM AEBSF, 0.5 mM benzamidine hydrochloride), lysed using a precooled EmulsiFlex-C5 homogenizer (Avestin) and clarified via centrifugation (16,000 g, 30 min, 4°C). Supernatant was passed through a HisTrap HP 5mL Ni2+ column (GE Healthcare) at 1 mL/min. The column was washed with 10 column volumes of chilled Ni2+ column buffer (50 mM TRIS pH 7.6, 500 mM NaCl, 10% (v/v) glycerol, 50 mM imidazole, 2 mM β-mercaptoethanol) before elution with Ni2+ column buffer supplemented with 400 mM imidazole. Proteinaceous fractions were then separated on a HiLoad 16/600 Superdex 200 gel filtration column (GE Healthcare) pre-equilibrated with size exclusion column buffer (SEC buffer; 50 mM TRIS pH 8.0, 150 mM NaCl, 2 mM tris(2-carboxyethyl) phosphine (TCEP)). AMPK-containing fractions were pooled and concentrated to ∼2 mg/mL using Amicon centrifugal filter units (Merck Millipore), flash frozen in liquid N2 and stored at −80°C. Purified AMPK subunits were validated by time of flight-mass spectrometry (ToF-MS) and sample purity confirmed by SDS-PAGE. CaMKK2 was expressed as an FLAG-tagged fusion in Sf21 cells as previously described.[62] Sf21 insect cells were infected at a multiplicity of infection of 10 and harvested 72 h post-infection. Cell lysates were prepared as for recombinant AMPK, and CaMKK2 was purified on anti-FLAG M2 affinity gel (Sigma-Aldrich). Protein was eluted with 50 mM Tris-HCl, pH 7.4, 100 mM NaCl, 0.25 mg/mL FLAG peptide (DYKDDDDK), flash frozen in liquid N2 and stored at −80°C.

Thermal melt shift assay

Reactions were set up in final volumes of 20 μL in 0.2 mL skirted 96-well PCR plates (Thermo Fisher) containing 2 μL of 20x SYPRO Orange (Thermo Fisher) dye, 14 μL of SEC buffer, and 4 μL of AMPK at 1 mg/mL (∼1.5 μM final concentration). After mixing, the plate was sealed with Microseal "B" (Bio-Rad) and centrifuged at low speed (1,000 g, 1 min). The thermal melt was then immediately performed on a CFX96 Real-Time PCR System (Bio-Rad) controlled by the CFX manager software (Bio-Rad; v3.1) with the scan mode set to FRET and plate type set to BR white. Temperature was increased in increments of 0.2°C from 10°C to 95°C at a ramp rate of 0.5°C/min. Data were analyzed in the Bio-Rad CFX manager software, where the first derivative of the relative fluorescence unit (RFU) melt curve was taken (-d(RFU)/dT) to generate the melt peak. This was visualized in negative mode and the melting temperature (Tm) was taken at the global minima.

In vitro phosphorylation assay

200 ng of his-tagged α1β1γ1 or α1β1(G2A)γ1 was incubated with 20 ng CaMKK2 in the presence of 50 mM Tris-HCl (pH 7.4), 150 mM NaCl, 10% glycerol, 0.02% Tween 20, 2 mM $MgCl_2$ and 200 μM ATP at 32°C. Reactions were terminated after the specified time by addition of SDS sample buffer and immunoblotted for phosphorylation of α1-Thr172.

Immunoprecipitation

5 μL of AMPKβ1 (Signalway Antibody), 5 μL PP1MA (ab14824, Abcam), or 2 μg PP1MB (13193-1, Proteintech Group) antibody was coupled to 5 μL of packed Protein G Sepharose beads (GE Healthcare). 200 μg protein lysate was added to the beads-antibody conjugate and the tubes were incubated on a vibrating shaker (Vibramax) at 4°C overnight. The beads/immune-complex were washed 3 times with cold lysis buffer and resuspended in 25 μL of 1x SDS sample buffer and boiled at 95°C for 5 min. The eluted proteins were separated by SDS-PAGE followed by immunoblotting.

Immunofluorescence

For immunofluorescence, glass coverslips with thickness No 1.5 (Epredia) were coated with collagen solution (125-50, Sigma) for 30 min at 37°C and then each coverslip was placed in one well of 24-well plates. 7 x 10^4 cells were plated per well in 24-well plates containing the coated coverslips. Cells were incubated with AICAR (2 mM) or vehicle for 1 h, followed by fixation in 4% formaldehyde (prepared by dilution of 37% formaldehyde (Sigma-Aldrich) in PBS) for 15 min at room temperature. Cells were washed 3x with PBS-Triton X-100 (0.01%), permeabilized and blocked with PBS-Saponin (0.1%) containing 5% BSA for 1 h at room temperature. Solution was aspirated and primary antibody against LAMP1 (DSHB) diluted in 5% BSA in PBS-Triton X-100 (0.01%) at a concentration of 2 μg/mL, was added to the cells and incubated in the dark at room temperature for 2 h. At the end of the incubation time, the solution containing the LAMP1 antibody was removed and the cells were washed one time with PBS-Triton X-100 (0.01%). Primary antibody against AMPKβ1 (Signalway Antibody) was diluted in 5% BSA in PBS-Triton X-100 (0.01%) at 1:100 dilution and incubated overnight at 4°C in the dark. Next day, cells were washed 3x with PBS-Triton X-100 (0.01%), 5 min each. Secondary antibodies (anti-rat, Alexa Fluor 647, Thermo Fisher, A-21247, and anti-mouse, Alexa Fluor 488, Thermo Fisher, A-11001) diluted in PBS-Triton X-100 (0.01%) at

1:500 dilution were added to the cells and incubated for 1 h at room temperature in dark. Cells were washed 3x with PBS-Triton X-100 (0.01%), 5 min each. To stain nuclei, Hoechst 33258 (Sigma-Aldrich) diluted 1:500 in PBS was added to the cells and incubated for 5 min at room temperature. Cells were washed 3x with PBS and mounted using Fluoromount G mounting medium (Sigma-Aldrich). Image acquisition was done on a Carl Zeiss LSM 780 confocal microscope with 63× objective using same settings for each condition.

Image analysis was performed using the Fiji version of the image software ImageJ[63] on raw images after conversion to 8-bit format. Regions of interest (ROIs) of whole cells were defined after automatic thresholding using the Otsu method on the AMPK β1 image. After background subtraction and clearing of areas outside ROIs colocalization analysis was performed using the JACoP plugin[64] with manual thresholding. Briefly, the threshold value for the AMPK β1 image was determined using the fluorescence signal intensity from AMPK β1 KO cells stained and imaged in the same batch. Manual thresholding for the LAMP1 image was performed using thresholds that define lysosomal structures. The same defined thresholds for AMPK β1 and LAMP1 were applied to all images within the same batch. JACoP was used to calculate Manders' coefficients,[65] the fraction of colocalized pixel intensities in areas of LAMP1 or AMPK β1 fluorescence tM1 and tM2, respectively.

c-Fos immunohistochemistry

20-week-old HFD-fed male mice were fasted overnight (16 h) and anesthetized by ketamine/xylazine injection followed by transcardial perfusion with 4% paraformaldehyde. Brains were dissected, postfixed overnight at 4°C and placed in 25% sucrose solution before cryostat sectioning. Sections were cut at 30 μm thickness throughout the entire brain and stored in cryoprotectant at −20°C. For immunohistochemical staining, every fourth section was selected, washed in PBS and blocked for 2 h at room temperature with 5% normal goat serum in 0.2% Triton X-100/PBS. Sections were incubated with c-Fos rabbit polyclonal IgG (Abcam) overnight at 4°C at 1 : 1000 in 2% normal goat serum/0.1% BSA/0.2% Triton X-100/PBS. Following 3x washes with 0.2% Triton X-100/PBS, sections were incubated with polyclonal goat anti-rabbit IgG conjugated to DyLight 488 (ab96899, Abcam) for 2 h at room temperature at 1 : 200 in 2% normal goat serum/0.1% BSA/0.2% Triton X-100/PBS. After 2 x washes with 0.2% Triton X-100/PBS, sections were coverslipped using Fluoroshield mounting medium (Sigma-Aldrich). Guided by the mouse brain atlas by Franklin and Paxinos,[66] we identified 4-6 random sections per brain through each nucleus of interest from bregma −1.34 mm to −1.94 mm and visualized cells using a Leica Thunder DMi8 microscope relayed by a Leica DFC9000 CMOS camera. c-Fos positive cells within each nucleus were counted using ImageJ software.

siRNA knockdown

siRNA knockdown was carried out using Lipofectamine RNAiMAX transfection reagent (Invitrogen). Briefly, cells were seeded in a 6-well plate a day before transfection. Next day, indicated siRNAs were introduced into cells as per the manufacturer's instructions. Cells were harvested 48 h post-transfection for analysis.

Proximity ligation assay

Proximity ligation assay was carried out using Duolink In Situ Red Starter Kit Mouse/Rabbit (Sigma-Aldrich) following manufacturer's instruction. Briefly, 2.5 x 10^4 cells per well were seeded in a μ-slide angiogenesis chamber (Ibidi). 24 h later, cells were fixed in 4% paraformaldehyde for 15 min at room temperature. Cells were washed 3x with PBS-Triton X-100 (0.01%), permeabilized and blocked with PBS-Saponin 0.1% containing 5% BSA for 1 h at room temperature. Primary antibodies diluted in Duolink antibody dilution buffer (1:100 AMPKβ1 (#27201, Signalway Antibody), 1:250 PPM1A (#12961-1, Proteintech Group) and 1:250 PPM1B (#13193-1, Proteintech Group). were added to cells and incubated at 4°C overnight protected from light. Next day, cells were washed 3x with PBS-TritonX, 5 min per wash. Proximity Ligation Assay probes (Rabbit Plus and Mouse Minus) diluted in antibody dilution buffer were added and incubated at 37°C for 1 h protected from light. Cells were washed 2x with PBS-Triton X-100, 5 min each wash. 15 μL ligation mix was added in each well and incubated at 37°C for 30 min, followed by a washing step. 15 μL amplification mixture was added in each well and incubated at 37°C for 100 min protected from light. Cells were washed 2x with PBS-Triton X-100, 5 min each wash. 15 μl mounting medium containing DAPI was added in each well. Image acquisition was done on Leica SP8 confocal microscope using same settings for each condition. Images were processed and analyzed in Fiji/ImageJ using the Common Tools Plugin (BioImaging And Optics Platform, École polytechnique fédérale de Lausanne). For quantification of mean intensity and number of spots per cell, an ImageJ script was used to define the Hoechst-stained nucleus as Region of Interest (ROI) in each cell and required parameters from the Red channel was measured for each ROI (cell).

Click chemistry

To assess myristoylation of AMPKβ1 or PP1MA/B click chemistry was performed using Click-iT myristic acid, azide (12-azidododecanoic acid) kit (Thermo Fisher). Briefly, 1 x 10^6 cells were plated in a 10-cm dish and experiments were performed when cells were 80% confluent. Cells were washed with PBS and fresh complete medium containing indicated concentrations of myristic acid-azide was added and incubated at 37°C for indicated time points. Cells were lysed and AMPKβ1 or PPM1A/B were immunoprecipitated from cell lysates (500 μg) as described. The immunoprecipitates were subjected to click chemistry reaction using the Click-iT protein reaction buffer kit (Thermo Fisher). Briefly, 40 μM biotin-alkyne solution was added to the immunoprecipitates followed by $CuSO_4$ solution and the reaction additives provided in the kit. The proteins were subjected to methanol:chloroform (4:1) precipitation and

centrifuged for 5 min at 13,000g. The upper aqueous phase was discarded leaving the interface layer containing the protein precipitate intact. 450 μL methanol was added to the tube, vortexed and centrifuged for 5 min at 13,000g to pellet the protein. The pellet was washed with 450 μL methanol to remove the residual reaction components. The pellets were allowed to air-dry. The dried protein precipitates were resolubilized in Laemmli sample buffer, separated by SDS-PAGE and subjected to immunoblotting using the Odyssey nitrocellulose membranes (LI-COR). The membranes were blocked in Tris-buffered saline/0.1% Tween 20 containing 5% BSA for 1 h and incubated in Streptavidin AlexaFluor conjugates (AF488, Thermo Fisher, #S11223 or AF680, Thermo Fisher #S21378) diluted at 1:10,000 in the blocking buffer at 4°C overnight. Membranes were scanned using Odyssey CLx Infrared Scanner.

Gene expression analysis

For mRNA expression analysis, liver and adipose tissue from 20 to 24-week-old mice were homogenized in Tri-Reagent (Sigma-Aldrich) and RNA isolated as per manufacturer's instructions. 500 ng of RNA was used to generate cDNA using the SuperScript IV Reverse Transcriptase Synthesis System (Thermo Fisher). The PCR reaction was performed using the AmpliTaq Gold DNA Polymerase Kit (Thermo Fisher) and specific TaqMan Gene Expression Assays (Thermo Fisher) on a Corbett Rotorgene 3000 (Corbett Research). The critical threshold (Ct) was manually set in the exponential phase and the Ct values determined by the Corbett Rotorgene instrument software. Relative expression was calculated using the comparative Ct ($2^{-\Delta\Delta Ct}$) method and normalized to eukaryotic 18S rRNA for liver samples and *Actb* for adipose tissue analysis.

AMPK activity assays

For AMPK activity assays, total AMPKα (pan-α antibody[67]) or AMPKα1 (custom-made antibody[28]) was immunoprecipitated overnight at 4°C from 1 mg of liver tissue homogenate or 250 μg of MEF cell lysates pre-conjugated to Protein-A Agarose or Protein-G Sepharose beads, respectively. The immunoprecipitates were subjected to *in vitro* kinase assay as previously described in detail.[36]

De novo lipogenesis and fatty acid oxidation assays

Primary hepatocytes were isolated by collagenase perfusion and maintained in Medium 199 supplemented with 10% fetal bovine serum as previously described.[68] The following day, cells were cultured for 2 h in serum-free M199 followed by incubation with 5 μCi/mL [^{3}H] acetate (sodium) (PerkinElmer) and 0.5 mM sodium acetate for 3 h. Medium was then removed and cells washed with PBS before lipid extraction using chloroform:methanol (2:1). For determination of triglyceride synthesis, the lipid fraction was removed, dried using a SpeedVac vacuum concentrator and redissolved in chloroform:methanol (2:1) supplemented with triglyceride standard (Sigma-Aldrich) before separation on thin-layer chromatography (TLC) UNISIL silica GF plates (Analtech) in heptane:isopropylether:glacial acetic acid, 60:40:3. Plates were sprayed with dicholoroflurescein (0.02% w/v in EtOH) to visualize lipids and the triglyceride fraction was removed for liquid scintillation counting using a Tri-Carb 4810TR Liquid Scintillation Analyzer (PerkinElmer). Triglyceride synthesis rates were calculated as nmol of ^{3}H-labeled acetate incorporated per milligram of cell protein per hour.

For fatty acid oxidation experiments, hepatocytes were incubated in serum-free Medium 199 for 2 h followed by incubation with 0.5 μCi/mL [1-^{14}C]palmitic acid (PerkinElmer), 0.25 mM palmitate (conjugated to 2% BSA) and 1 mM carnitine for 4 h. Medium was removed and cells acidified with 5% $HClO_4$ for 45 min at room temperature. The acid precipitate was removed by centrifugation and radioactivity of the supernatant measured by liquid scintillation counting to determine ^{14}C incorporation into acid soluble metabolites (ASM). Oxidation rates were calculated as nmol of ^{14}C-labeled ASM per milligram of cell protein per hour.

QUANTIFICATION AND STATISTICAL ANALYSIS

All data are presented as mean ± s.e.m. and subjected to statistical analysis using GraphPad Prism 9 software. Immunoblots were analyzed using Image Studio Light V5.2 (LI-COR Biosciences) software. Immunofluorescence images were analyzed using Fiji version of the image software ImageJ.[63] Sample size was estimated from our previously published studies.[68,69] Statistical significance was determined using two-tailed unpaired Student's t-test for a single variable unless otherwise stated. 1) Age-dependent body weight and body composition changes of mice on chow or HFD, 2) time-dependent metabolic parameters measured in CLAMS and 3) changes in blood glucose concentrations in tolerance tests were analyzed by repeated measures two-way ANOVA followed by Šídák's post-hoc test. To evaluate the effect of body composition on energy expenditure, linear regression analysis and analysis of covariance (ANCOVA) with lean mass as covariate was performed using CalR.[70] All remaining data comparing two variables (genotype, treatment) were analyzed by ordinary two-way ANOVA with Šídák's post-hoc test. Significance was accepted at $p < 0.05$.